JGR Space Physics

RESEARCH ARTICLE
10.1029/2025JA033769

Key Points:

- Geomagnetic disturbances (GMDs) can be identified in auroral movements and intensifications observed with high altitude ultraviolet imagers
- The observed pre-midnight GMDs are associated with highly localized and transient up/down current pairs and localized electrojets
- GMDs and their associated currents often vary on the scale of a few tens of seconds, suggesting the importance of high cadence images

Supporting Information:

Supporting Information may be found in the online version of this article.

Correspondence to:

M. J. Engebretson,
engebret@augsburg.edu

Citation:

Engebretson, M. J., Mende, S. B., Weygand, J. M., Kebede, E. H., Ochoa, J. A., Tian, S., et al. (2025). IMAGE satellite and ground-based magnetometer observations of large geomagnetic disturbances and rapid variations in ionospheric and vertical currents. *Journal of Geophysical Research: Space Physics*, *130*, e2025JA033769. https://doi.org/10.1029/2025JA033769

Received 21 JAN 2025
Accepted 18 JUL 2025

Author Contributions:

Conceptualization: Mark J. Engebretson, James M. Weygand
Data curation: Stephen B. Mende, Erik S. Steinmetz, Jesper W. Gjerloev
Formal analysis: Mark J. Engebretson, James M. Weygand, Sheng Tian
Funding acquisition: Mark J. Engebretson, James M. Weygand
Investigation: Mark J. Engebretson, James M. Weygand, Ethiopia H. Kebede, Jesus A. Ochoa, Sheng Tian, Mark B. Moldwin, Michael D. Hartinger, Chigomezyo M. Ngwira
Methodology: Mark J. Engebretson, James M. Weygand

IMAGE Satellite and Ground-Based Magnetometer Observations of Large Geomagnetic Disturbances and Rapid Variations in Ionospheric and Vertical Currents

Mark J. Engebretson[1], Stephen B. Mende[2], James M. Weygand[3], Ethiopia H. Kebede[1], Jesus A. Ochoa[1], Sheng Tian[4], Erik S. Steinmetz[1], Mark B. Moldwin[5], Michael D. Hartinger[6], Chigomezyo M. Ngwira[7,8], and Jesper W. Gjerloev[9]

[1]Department of Physics, Augsburg University, Minneapolis, MN, USA, [2]Emeritus Space Science Laboratory, University of California, Berkeley, CA, USA, [3]Department of Earth Planetary and Space Sciences, UCLA, Los Angeles, CA, USA, [4]Department of Atmospheric and Oceanic Sciences, UCLA, Los Angeles, CA, USA, [5]Department of Climate and Space Sciences and Engineering, University of Michigan, Ann Arbor, MI, USA, [6]Space Science Institute, Boulder, CO, USA, [7]Department of Physics, Catholic University of America, Washington, DC, USA, [8]Heliophysics Division, NASA Goddard Space Flight Center, Greenbelt, MD, USA, [9]Johns Hopkins University Applied Physics Laboratory, Laurel, MD, USA

Abstract Ultraviolet images of Earth's polar regions obtained by high altitude spacecraft have proved to be immensely useful for documenting numerous features of the aurora and understanding the coupling between Earth's magnetosphere and ionosphere. In this study we have examined images obtained by the far ultraviolet Spectrographic Imager camera on the IMAGE satellite during the first three years of its mission (2000–2002) for comparison with observations of large geomagnetic disturbances (GMDs) by ground-based magnetometers in eastern Arctic Canada. To our knowledge, this is the first study to investigate the use of high-altitude imager data to identify the global context of GMDs. We found that rapid auroral motions or localized intensifications visible in these images coincide with regions of large *dB*/*dt* as well as localized and closely spaced up/down vertical currents and increased equivalent ionospheric currents, but one of the two events presented did not appear to be related to substorm processes. These magnetic perturbations and currents can appear or disappear in a few tens of seconds, thus highlighting the importance of images with a high cadence.

1. Introduction

Earth's high latitude ionosphere contains a mixture of neutral gas and plasma that is energized from several directions: from below by atmospheric tides, from above by spatially and temporally varying distributions of plasma waves, electric currents, and precipitating energetic charged particles from the magnetosphere, and during daytime hours by ultraviolet and X-ray photons emitted by the Sun. The only feature of this complex region open to investigation before the space age was the aurora, which are created by a complex mixture of ion and neutral particle interactions and photochemical reactions driven by these inputs. We now understand that the dynamical processes that produce the visible aurora also generate a variety of waves, including physical motions of the neutral atmosphere, plasma waves with a wide range of frequencies (10^{-3} to $>10^{6}$ Hz), and ultraviolet, visible, and infrared light with specific wavelength distributions. Ground-based cameras deployed throughout high-latitude regions can detect visible light in limited geographic regions during nighttime, but most of the ultraviolet and infrared waves of interest are blocked by the atmosphere below. Satellites orbiting above the ionosphere and capable of viewing ultraviolet emissions, however, have observed the detailed structure of the aurora, and high-altitude spacecraft such as Dynamics Explorer (e.g., Frank & Craven, 1988), Viking (e.g., Marklund et al., 1987), Polar (e.g., Germany et al., 1997), and IMAGE (e.g., Mende, Heetderks, Frey, Lampton, et al., 2000; Mende, Heetderks, Frey, Stock, et al., 2000) provided increasingly detailed auroral images from apogee with a field of view of the full Earth.

Images from both low-orbiting and high-altitude spacecraft have made significant contributions, often in conjunction with other instrumentation, to developing a quantitative understanding of many features of the interactions between the magnetosphere, ionosphere, and lower atmosphere, including both geomagnetic storms and substorms. Data from the IMAGE spacecraft have contributed to studies of substorm onsets (e.g., Frey et al., 2004) and recovery phases (e.g., Mende et al., 2002), quantifying input proton and electron energy characteristics and their consequent ionospheric composition changes (Hubert et al., 2002), detached auroras triggered

by sudden solar wind dynamic pressure enhancements (e.g., Zhang et al., 2003), the association of proton arcs and ULF waves with auroras at subauroral latitudes (e.g., Immel et al., 2005), and upward ion flows with the highest energy outflow corresponding to the brightest auroral arcs (e.g., Kistler et al., 2002). However, since the end of the IMAGE mission in 2005 and the Polar mission in 2008, no high-altitude Earth-orbiting research spacecraft has been equipped with such imagers.

The realization that geomagnetic storms could produce large transient electric fields at Earth's surface was first stimulated by the occurrence of large, rapid changes in the geomagnetic field at the ground level during the great magnetic storm of 1859 (Carrington, 1859), which were accompanied not only by bright auroras that extended to middle and even low latitudes but also by large induced voltages in long distance telegraph lines. More recent extreme magnetic storms and their damaging consequences were reviewed by Hapgood (2019), Boteler (2019), and Love et al. (2019). Studies focusing on large, isolated magnetic perturbations with amplitudes $|\Delta B|$ of hundreds of nanotesla and 5- to 10-min duration (denoted magnetic perturbation events—MPEs—or geomagnetic disturbances—GMDs) and their consequent induction risks have been ongoing since at least 1997 (Boteler et al., 1998; Viljanen, 1997). Figure 2 of Engebretson, Pilipenko, et al. (2019) shows three examples of such GMDs. Although many subsequent studies have focused on GMDs during geomagnetic storms that can extend to lower latitudes (e.g., Kappenman, 2001), recent studies have demonstrated that over several solar cycles most large (Milan et al., 2023) and extreme (Engebretson, Yang, et al., 2024) GMDs occurred in the auroral zone, and could occur during both storm and non-storm times.

Event studies of GMDs routinely incorporate both arrays of ground-based auroral imagers and magnetometers (e.g., Engebretson, Gaffaney, et al., 2024; Ngwira et al., 2025; Weygand et al., 2021) to characterize the association of GMDs with spatial and temporal variations in the aurora. This study is motivated by our interest in determining whether high-altitude satellite images of the aurora could not only be clearly associated with these events but also provide a wider spatial context for them, and we confirm that this is the case. Our study thus anticipates the expected launch of the Solar wind Magnetosphere Ionosphere Link Explorer (SMILE) mission (Branduardi-Raymont et al., 2018) in late 2025, which will provide images of the UV aurora for the first time in almost two decades from a high-altitude spacecraft. It is also timely in that global satellite-based imagers (e.g., the Links mission) are a key component of missions recommended by the recently published Solar and Space Physics Decadal Survey (National Academies of Sciences et al., 2024).

We note that sparsely populated eastern Arctic Canada is not particularly vulnerable to damage from geomagnetically induced currents (GICs), which can be produced by GMDs that occur over regions with long-distance power lines and pipelines. No long-distance conductors are present in this region; instead, each of its towns has its own electrical power utility. However, the two-dimensional magnetometer coverage in eastern Arctic Canada has been useful for what is labeled "discovery research" in the 2024 Solar and Space Physics Decadal Survey (National Academies of Sciences et al., 2024) in many studies of high latitude phenomena including GMDs, especially in regard to their mesoscale features and physical causes (e.g., Engebretson, Gaffaney, et al., 2024; Runov et al., 2025).

Section 2 introduces the satellite-based imager and the ground-based magnetometers used in this study, and Section 3 presents two examples of auroral images that show localized and rapidly varying auroral activity in close spatial and temporal proximity to large GMDs—one during very quiet geomagnetic conditions, and the other during the recovery phase of a moderate magnetic storm. These examples also show that GMD-related activity is highly variable on scales of tens of seconds, so that a rapid cadence of auroral images is necessary to adequately characterize it. Section 4 discusses some of the implications of these observations and Section 5 summarizes our findings.

2. Instrumentation

The IMAGE spacecraft (Burch, 2000) was launched on 25 March 2000 and placed in a 1,000 km × 46,004 km highly elliptical orbit around the Earth, with an initial inclination of 90.01° (passing over the poles) and a 14.2-hr period. For ultraviolet and neutral atom imaging, the time resolution is set by the ~2.05 min spin period of the IMAGE spacecraft.

The dual-channel spectral imager on the far ultraviolet Imager (FUV) on this spacecraft provided spectral imaging of the aurora near Lyman-α and at OI (135.6 nm) wavelengths, capturing a 5-s exposure each satellite revolution

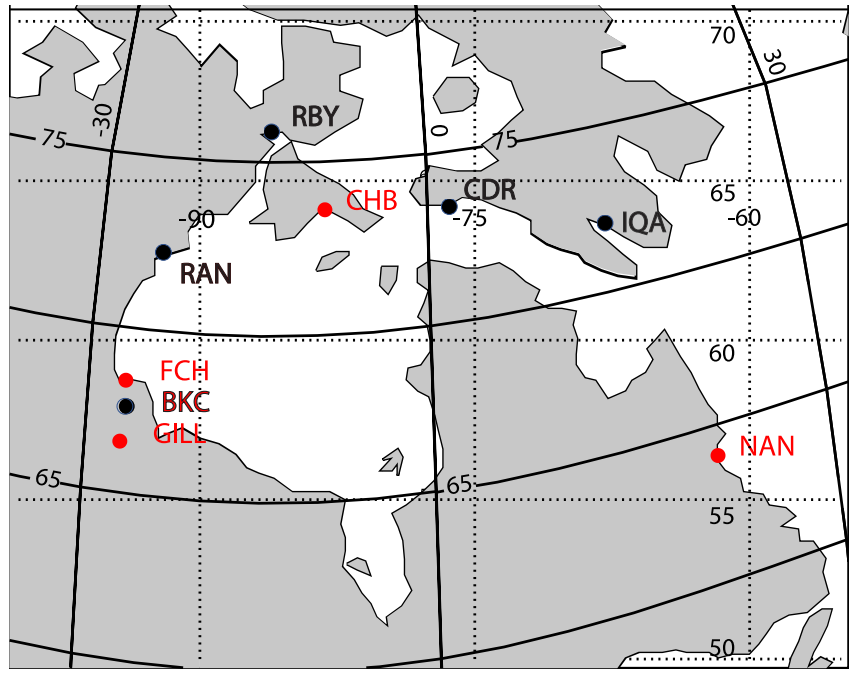

Figure 1. Map of the ground magnetometer stations (red dots) used for the two events presented here. Dotted lines show geographic latitude and longitude, and solid lines show corrected geomagnetic latitude and longitude. Other stations in this region listed above are indicated by black dots.

(Mende, Heetderks, Frey, Lampton, et al., 2000; Mende, Heetderks, Frey, Stock, et al., 2000). The SI-13 channel used in this study has a passband of 5 nm around the 135.6 nm doublet line of oxygen OI emission, but the measured signal also includes a relatively small amount of UV from bands of the N2 LBH emission (Frey et al., 2001). The raw SI-13 signal is, however, adequate for qualitative studies of auroral activity, as is done here. The SI-12 channel is sensitive to the Doppler-shifted Lyman-α hydrogen emissions near 121.8 nm generated by the incoming neutral hydrogen caused by proton precipitation while rejecting the non-Doppler-shifted geocoronal Lyman- α.

Vector magnetometer data used in this study were recorded at high magnetic latitude stations in the Magnetometer Array for Cusp and Cleft Studies (MACCS, Engebretson et al., 1995) and the Canadian Array for Realtime Investigations of Magnetic Activity (CARISMA, Mann et al., 2008) arrays in Eastern Arctic Canada, as detailed in Figure 1 and Table 1. MACCS data were sampled at a 0.5 s cadence, and CARISMA data were provided at a 5 s cadence. All magnetometer data are presented in local magnetic coordinates with sensor axes oriented as follows: X: magnetic north, Y: magnetic east, and Z: vertically down. Derivatives of each component of the magnetic field data were obtained using the three-point Lagrangian approximation (Engebretson, Yang, et al., 2024).

During the two events presented here the number of working magnetometer stations was much less than is the case currently. To the best of our knowledge, the MACCS magnetometer at Nain was the only instrument on the coast of Labrador. Data were available from the Intermagnet station at Iqaluit in southeastern Baffin Island, but its variations were more than an order of magnitude smaller, consistent with the absence of any significant nearby auroral emissions. During the second event, no useful data were available from the two other CARISMA stations along the west coast of Hudson Bay (Back Lake had no data, and Rankin Inlet had almost all fill data), and there were also no data from the MACCS stations Cape Dorset or Repulse Bay situated toward the east and north of Hudson Bay.

This study also makes use of Spherical Elementary Currents Systems (SECS) maps (Amm, 1997; Amm & Viljanen, 1999; Amm et al., 2002) produced using all available ground-based magnetometers in northern North America and western Greenland (Weygand, 2009a, 2009b; Weygand et al., 2011), as shown in the example in Figure 5. These maps show the equivalent ionospheric horizontal currents and vertical upward and downward current intensities (a proxy for field-aligned currents).

Table 1
Locations of the Magnetometer Stations Used for the Two Events Presented Here

Array	Station	Code	Geog. lat.	Geog. lon.	CGM lat.	CGM lon.	UT of mag midnight
MACCS	*Coral Harbour*	*CHB*	64.2°	276.7°	74.1°	−9.9°	05:26
	Nain	*NAN*	56.4°	298.3°	64.6°	22.1°	03:22
	Cape Dorset	CDR	64.2°	283.4°	73.8°	1.7°	04:39
	Repulse Bay	RBY	66.5°	273.8°	76.2°	−15.3°	05:48
CARISMA	*Fort Churchill*	*FCH*	58.8°	265.9°	68.8°	−27.4°	06:37
	Gillam	*GILL*	56.4°	265.4°	66.5°	−27.8°	06:39
	Back Lake	BKC	57.7°	265.8°	67.7°	−27.4°	06:37
	Rankin Inlet	RAN	62.8°	267.9°	72.6°	−25.0°	06:27
Intermagnet	Iqaluit	IQA	63.8°	291.5°	72.7°	14.7°	03:49

Note. Geographic and corrected geomagnetic (CGM) latitude and longitude are shown, as well as the universal time of local magnetic midnight. Stations with data used in this study are italicized. CGM coordinates were calculated at 100 km altitude for (a) 22 December 2000 for Nain and Iqaluit, and (b) 20 April 2002 for the remaining stations, using http://sdnet.thayer.dartmouth.edu/aacgm/aacgm_calc.php#AACGM, last accessed 10 April 2025.

The SECS method first produces the equivalent ionospheric currents by removing a background magnetic field from the ground magnetometers and then inverting the remaining magnetic field fluctuations through singular value decomposition to obtain the equivalent currents. For the most part these equivalent currents are Hall currents, but contribution from other currents such as the Pedersen and field aligned currents can enter into the equivalent current estimates because the ionosphere has non-uniform conductivity. Auroral images and particle precipitation data indirectly indicate that the ionospheric conductivity is non-uniform, but we do not need to know the distribution or values of the conductivity to obtain the equivalent currents. See Amm and Viljanen (1999) for more details. The second part of the SECS method is to obtain the curl-free currents, which the SECS method refers to as current amplitudes (field-aligned-like currents), because they are vertical currents derived at pre-determined ionospheric grid points. These current amplitudes are calculated from the curl of the equivalent ionospheric currents. To obtain these results from Ohm's law in the ionosphere, we make two assumptions. The first assumption is that the Hall to Pedersen conductance ratio is constant: $\alpha = \Sigma_H/\Sigma_P = \text{constant}$ where Σ_H and Σ_P are the height integrated Hall and Pedersen conductivities. The second assumption is that $\left(\nabla\Sigma_H \times \vec{E}\right)_r = 0$, where $\vec{E}$ is the convection electric field. From these two assumptions, Ohm's law can be simplified and the current amplitudes can be written as

$$j_{df,r} = \nabla \cdot \vec{J} = -\frac{1}{\alpha}\left(\nabla \times \vec{J}_{df}\right)$$

where $\vec{J}_{df}$ is the divergence free current (equivalent current) and $j_{df,r}$ is the current amplitude (vertical current/field aligned like current). For more details on the derivation, see Amm et al. (2002), Juusola et al. (2009), and Vanhamäki and Amm (2011).

Validation of the SECS-derived vertical currents was provided by Weygand and Wing (2016) and Weygand et al. (2023). Weygand and Wing (2016) compared the location of the region-1 and region-2 boundary obtained by the DMSP spacecraft with the region-1 and region-2 boundary observed in the SECS current amplitudes, and found that the boundaries typically agreed within 0.2° ± 1.3°, indicating that the location of the region-1 and region-2 boundary can reasonably be determined from ground magnetometer data. Weygand et al. (2023) overlaid the equivalent ionospheric current pattern over North America on the field-aligned current pattern based on Active Magnetosphere and Planetary Electrodynamics Response Experiment (AMPERE) measurements (Anderson et al., 2008), and found that the electrojets were situated between the AMPERE field-aligned currents. It is now commonly accepted that this technique can determine "vertical" currents as a proxy for field-aligned currents as well as instantaneous ionospheric equivalent currents, given a sufficiently dense set of ground-based magnetometers.

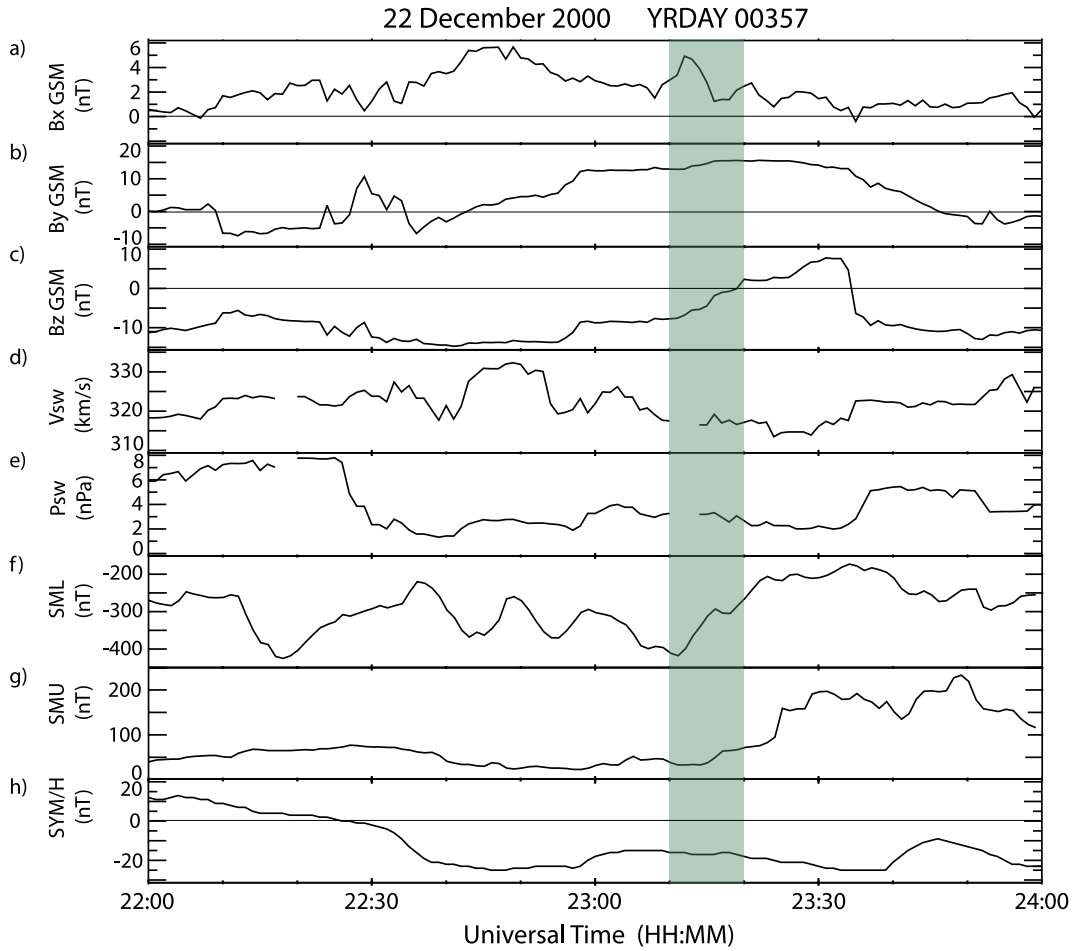

Figure 2. Time-shifted OMNI IMF and solar wind data (panels a–e) and the SML, SMU, and SYM/H magnetic activity indices (panels f–h) from 22:00 universal time (UT) to 24:00 UT 22 December 2000. The interval between 23:10 UT and 23:20 UT is shaded in green.

3. Observations

We identified >6 nT/s GMDs in data from all eight of the stations in the MACCS array and from selected CARISMA stations near Hudson Bay from the 25 March 2000 launch of the IMAGE spacecraft through the end of 2002. Of the 105 events identified, 49 occurred at Nain (64.4° MLAT), the only MACCS station at MLAT equatorward of 73.5°, and thus the station likely to be most often beneath the nominal location of the auroral zone. We then accessed the IMAGE SI data via the NASA CDAWEB database during each event. The majority of GMD events corresponded to no useful FUV images over this region for several reasons: the spacecraft's longitude was far from that of the magnetometer stations, the spacecraft was viewing the southern hemisphere or near the perigee, and/or there was no satellite data. Only eight days had both large GMDs and images with good viewing. Two events are presented here, one each occurring during quiet and disturbed geomagnetic conditions.

3.1. Event 1: 22 December 2000 23:13–23:18 UT

During this event, brief auroral intensifications occurred during otherwise relatively quiet geomagnetic conditions. Occurrence of a localized auroral region above Nain, on the east coast of Labrador, Canada, was simultaneous with large (up to ~8 nT/s) geomagnetic disturbances (GMDs) in all three magnetic field components between 23:13 universal time (UT) and 23:18 UT.

Figure 2 presents the larger context of this event. It shows time-shifted IMF and solar wind data from the NASA Science Data Portal (OMNI) database as well as the SuperMAG Low (SML) and SuperMAG Upper (SMU)

Table 2
Substorm Onsets Between 21:00 Universal Time (UT) and 24:00 UT on 22 December 2000 Included in the Newell and Gjerloev (2011), Frey et al. (2004), Frey and Mende (2006), Forsyth et al. (2015), and Ohtani and Gjerloev (2020) Substorm Lists Available on the SuperMAG Web Site and in the Mid-Latitude Positive Bay Index of Chu et al. (2015) and McPherron et al. (2015), McPherron and Chu (2018)

	Time (UT)	Onset location
Newell and Gjerloev	21:40	(Scandinavia 27°E)
Forsyth et al.	21:36	(Scandinavia 15°E)
	23:03	(Siberia 81°E)
	23:39	(Scandinavia 24°E)
Frey et al.	21:41	(Russia 52°E)
Ohtani and Gjerloev	21:41	(Scandinavia 27°E)
Chu et al.	22:13	No information
	23:35	No information

Note. Onset location and geographic longitude are presented when available.

auroral activity indices (SuperMAG versions of the AU and AL indices), and the SYM/H magnetic activity index for the interval from 22:00 UT to 24:00 UT on this day. The shaded interval from 23:10 UT to 23:20 UT includes the GMDs observed during this event. The IMF magnitude exceeded 10 nT during this entire 4-hr interval, with the largest components in the B_y and B_z directions (panels b and c); during the highlighted interval B_y was ∼+15 nT, and B_z rose from −7 to +3 nT. The solar wind velocity (V_{sw}) ranged between 315 and 332 km/s during the 4-hr interval, and was between 317 and 320 km/s during the highlighted interval (panel d). The solar wind pressure (P_{sw}) exceeded 6 nPa at 22:00 UT, but between 22:30 UT and 23:35 UT it varied only between 2 and 4 nPa, with a level of 3 nPa during the GMD events. The auroral zone magnetic activity shown in the SML (panel f) and SMU (panel g) indices was modest; SML varied between −180 and −430 nT and SMU varied between 40 and 240 nT, respectively, during the 22:00 UT to 24:00 UT interval. The SML index rose from −420 to −300 nT during the highlighted interval.

Table 2 shows substorm onsets between 21:00 UT and 24:00 UT that were included in the Newell and Gjerloev (2011), Frey et al. (2004), Frey and Mende (2006), Forsyth et al. (2015), and Ohtani and Gjerloev (2020) substorm lists available on the SuperMAG web site (Gjerloev, 2023) and in the Mid-latitude positive bay (MPB) index of Chu et al. (2015) and McPherron et al. (2015), McPherron & Chu (2018). Only two onsets occurred between 22:00 UT and the end of the GMD interval at 23:20 UT, and each appeared in only one substorm list: The onset at 22:13 UT in the MPB list coincided with a rapid 180 nT drop in SML beginning at 22:12 UT, and the onset at 23:03 UT in the Forsyth et al. list, 12 min before the larger of the two GMDs, coincided with a ∼70 nT drop in SML (Figure 2f). However, the Forsyth et al. list indicated that the onset at this time was at 81° east (in Siberia). Movie S1 in the Supporting Information, which shows successive FUV images from 22:00 UT to 23:52 UT, showed only weak and sporadic auroral activity propagating westward from Scandinavia across the Atlantic Ocean. In addition, SECS images between 23:03 UT and 23:20 UT (not shown) showed no evidence of a westward surge in the Greenland data.

Despite the strongly negative B_z component during most of the 4-hr interval, the SYM/H index (Figure 2h) remained at quiet levels during the 4-hr interval, never dropping below −25 nT, and it was −15 nT during the GMD events. The larger values of SYM/H between 22:00 UT and 22:30 UT and their subsequent drop may reflect the value and drop of P_{sw} during that same interval rather than a sign of the onset of a geomagnetic storm.

The top three panels (a–c and e–g) of each half of Figure 3 show three components of the magnetic field in local geomagnetic coordinates observed at Nain, and the bottom panels (d and h) show their derivative amplitudes on 22 December 2000. The left side presents the time series from 22:00 UT to 24:00 UT, showing only modest and slow variations between 22:00 UT and ∼23:10 UT. The right side shows more clearly the beginning of a negative bay in the B_x component at 23:12 UT, followed by a rapid drop in the B_x (north-south) component reaching a sharp minimum near 23:14:45 UT, and immediately rising rapidly toward its previous level. Variations in the B_z components were roughly similar in time although they were lower in amplitude, but the B_y component dropped most rapidly close to the time of minima in B_x and B_z. The largest derivative in each component (6.9 nT/s in B_x, −8.4 nT/s in B_y, and 4.9 nT/s in B_z) occurred within a few seconds of each other near 23:14:45 UT, as shown in panel h. Smaller derivative peaks occurred in B_x (−4 nT/s) at 23:13:50 UT and in B_x and B_y (∼2 nT/s) near 23:16:50 UT. Figure S1 in Supporting Information S1 shows the full daily magnetogram from Nain, and Table S1 in Supporting Information S1 contains the times and amplitudes of all three magnetic field components at Nain near the time of their GMD maxima.

Figure 4 shows an FUV satellite image of the aurora at 23:15:41 UT, recorded ∼1 min before the time when the brightest and most extensive auroral spot was observed above and slightly to the northwest of Nain. The auroral intensity is color-coded in pixel counts; the bright auroral region with counts from 30 to 70 per pixel ranged from slightly west of the middle of Labrador eastward into the North Atlantic Ocean, but at all other longitudes the pixel count in the auroral zone only very rarely exceeded 20.

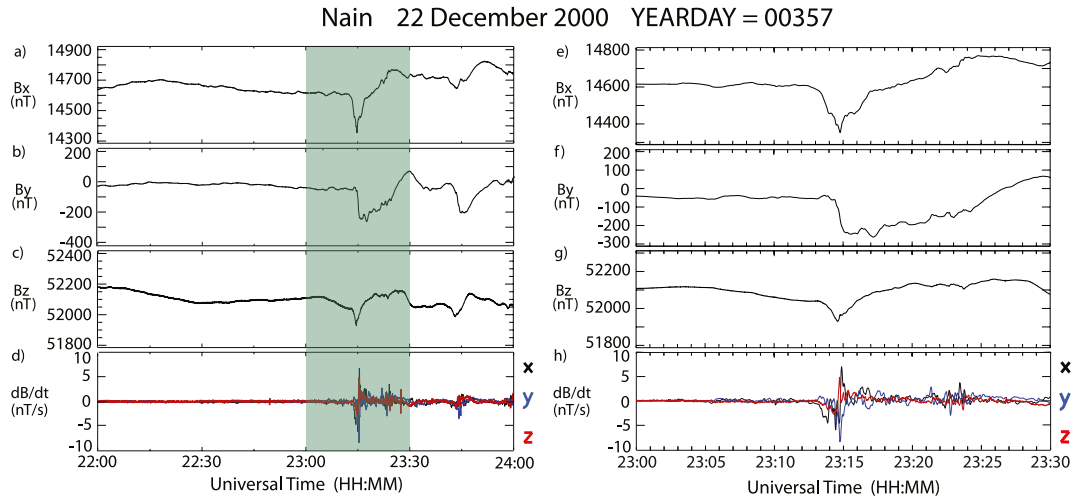

Figure 3. Magnetic field observations from Nain on 22 December 2000. Left side: 22:00 universal time (UT) to 24:00 UT. Right side: 23:00 UT-23:30 UT. Panels (a–c) and (e–g) show the B_x, B_y, and B_z components in local magnetic coordinates, and panels (d) and (h) show the color-coded derivatives of each component. The interval between 23:00 UT and 23:30 UT in the left-side panel is shaded in green.

Figure 5 shows a SECS map of the instantaneous equivalent ionospheric horizontal currents (black arrows) and vertical current intensities (upward in red, downward in blue) across North America and western Greenland at 23:14:30 UT on 22 December 2000. The stars show the locations of magnetometers providing data on this day, and the dots show the grid points at which the horizontal currents were calculated. This map shows very weak equivalent currents across most of Greenland and northern North America, but a localized up-down pair of strong vertical currents close to the location of Nain and a strengthened horizontal equivalent current between them and perpendicular to their axis.

A detailed description of the temporal evolution of the correlation between auroral intensity and SECS-derived vertical currents during the time interval from 23:00 UT to 23:30 UT on 22 December 2000 is provided in Figure 6. This figure shows one-dimensional time series plots of north-south and east-west cuts of both the auroral imager intensities (panels a and b) and the vertical current intensities (panels d and e), respectively, in what are designated as keogram and ewogram formats, from 23:00 UT to 23:30 UT on 22 December 2000. As noted above, each IMAGE SIE snapshot was for only 5 s. In order to increase the visibility of the auroral intensities, each horizontal bar is centered at the time of the beginning of a snapshot, but extends from 1 min before to 1 min after that time. The cadence of the SECS amplitudes in panels d and e is 10 s.

Figure 6a shows the time series of the auroral intensity observed between 50° and 80° MLat and in a range of 15° MLon centered at the location of Nain 22.1°, and Figure 6b shows the time series of the auroral intensity observed between −70° and +10° MLon and within ±7.5° MLat around the center MLat value of Nain, 64.6°. Figure 6c repeats the color-coded derivative plot of Figure 3h. Figures 6e and 6f show similar keogram and ewogram plots of the amplitude of SECS-derived vertical (upward and downward) currents. The green ovals and cross hairs in panels a, b, d, and e of Figure 6 denote the MLat, MLon, and UT of the peak *dB/dt* value observed at Nain shown in panel c.

Figure 6a shows that regions of increased auroral intensity passed near Nain at nearly constant latitude, while Figure 6b shows that regions of increased intensity moved into the longitudinal field of view from the east (higher MLon) and traveled westward. The most intense auroral region was overhead of Nain from ~23:13:30 UT to ~23:20 UT (the center times of the associated horizontal bars), which coincided approximately with the times of the largest derivatives in Figure 6c. A later interval of somewhat weaker derivatives from ~23:21 UT to ~23:24 UT was accompanied by weaker overhead aurora but may have been stimulated by the region of increased auroral intensity that appeared in the field of view from the east at 23:34 UT.

Figure 6d shows that upward (red) and downward (blue) currents intensified beginning near 23:13 UT, with downward currents north and upward currents to the south of Nain, but abruptly weakened near 23:14:40 UT.

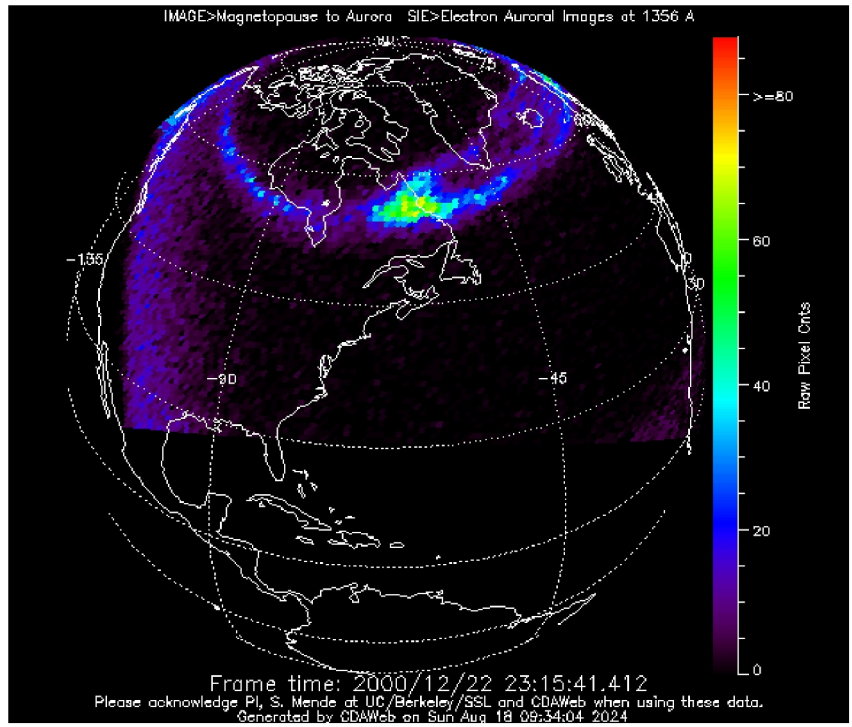

Figure 4. 1,356 Å auroral image from the IMAGE far ultraviolet Spectrographic Imaging camera at 23:15:41.412 universal time, 22 December 2000.

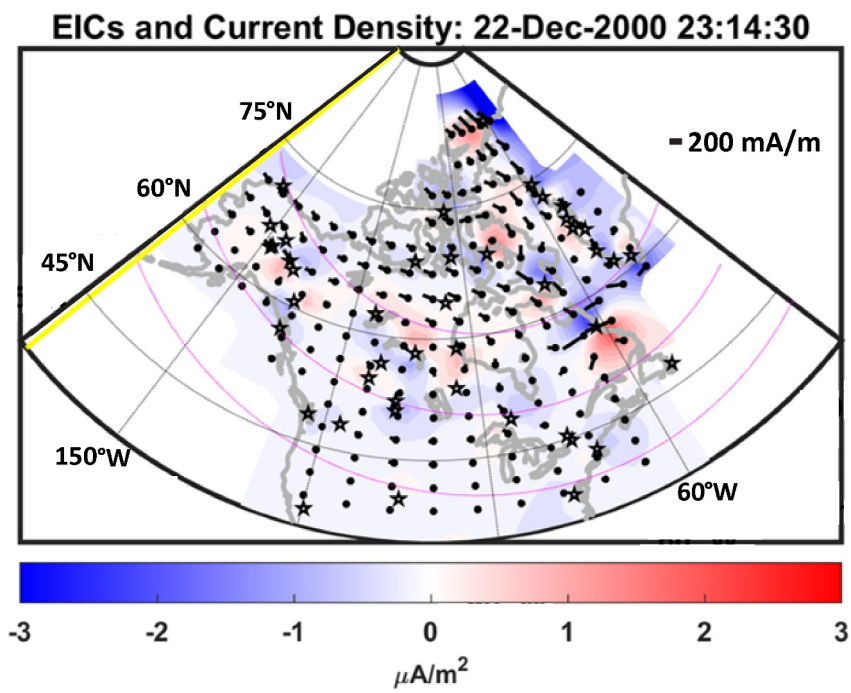

Figure 5. Spherical Elementary Current Systems map of the equivalent horizontal ionospheric currents (black arrows) and vertical current intensities (upward in red, downward in blue) across northern North America and western Greenland at 23:14:30 universal time, 22 December 2000. The stars show the locations of magnetometers providing data on this day, and the dots show the grid points at which the horizontal currents were calculated. The yellow line indicates the midnight meridian.

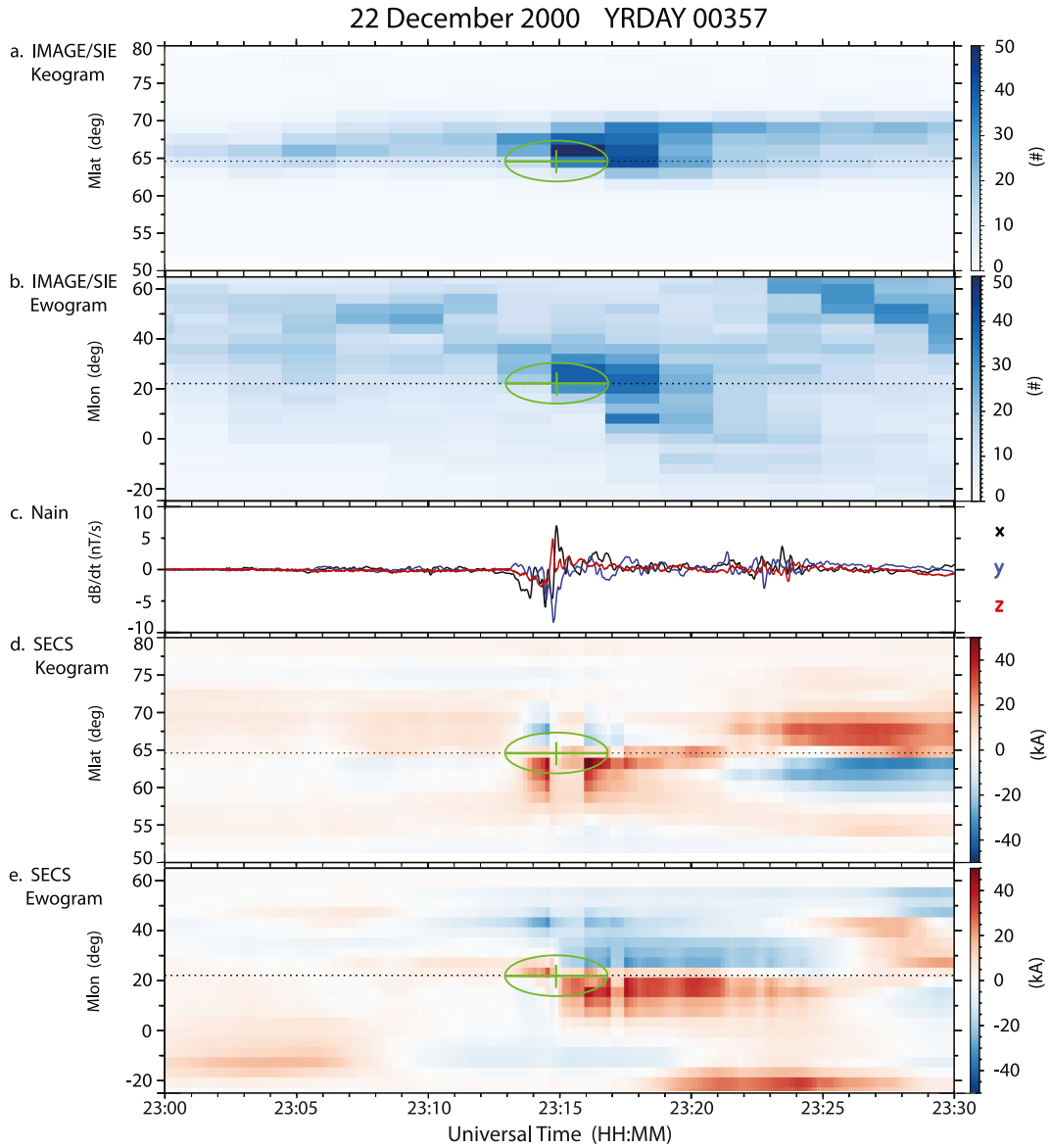

Figure 6. Panels (a) and (b) are keograms and ewograms of auroral intensity observed by the IMAGE SIE instrument between 23:00 universal time (UT) and 23:30 UT on 22 December 2000. Panel (c), a copy of Figure 3h, shows the color-coded derivatives of each component of the magnetic field at Nain. Panels (d) and (e) are keograms of the amplitude of SECS-derived vertical (upward and downward) currents. Both keograms (panels a and d) are calculated within ±7.5° around the −22.1° MLon of Nain, and the dashed lines show the 64.6° corrected magnetic latitude of Nain (vertical scale). Both ewograms (panels b and e) are calculated within ±2.5° around the 64.6° MLat of Nain, and the dashed lines show the −22.1° corrected magnetic longitude of Nain (vertical scale). In panels (a), (b), (d), and (e), the green ovals and cross hairs indicate the time of the peak *dB*/*dt* value shown in panel (c).

During this same interval Figure 6e shows that upward current appeared overhead and immediately east of Nain and downward current appeared ∼20° MLon to the east. These currents also abruptly weakened at 23:14:40 UT.

At 23:15 UT a weak upward current began to grow at the MLat of Nain at 23:15 UT (Figure 6d), and at the same time a downward current east of Nain and an upward current west of Nain began to grow (Figure 6e). At 23:15:50 UT, the intense currents that appeared north and south of Nain earlier in Figure 6d abruptly reappeared, and the currents east and west of Nain in Figure 6e abruptly intensified. Another sudden decrease in currents between 23:17 UT and 23:17:25 UT was evident in both Figures 6d and 6e. After this time the upward current in Figure 6d moved northward and the downward current became weaker, while the current pair in Figure 6e remained at their

previous longitudes. These changes in spatial patterns are consistent with rotations of a spatially localized current pair. At 23:21 UT, the currents rotated again, such that in Figure 6d an upward current was located north of Nain and a downward south of Nain, while their locations in longitude (Figure 6e) were unchanged. The variations in the intensity of these currents varied synchronously between 23:21 UT and 23:23 UT.

The times of increased derivative amplitudes in Figure 6c correspond approximately to the times of changing amplitudes of vertical currents in Figures 6d and 6e. The peak dB/dt values near 23:14:50 UT appeared shortly after the abrupt weakening of these currents near 23:14:40 UT, the increased dB/dt values near 23:16:10 UT appeared shortly after the abrupt increase in these currents at 23:16 UT, and the increased dB/dt values between 23:21 UT and 23:24 UT peaked shortly after variations in the vertical currents during this same time span. The reduced amplitude of the derivatives in Figure 6c after 23:24 UT is also consistent with the constant or only slow changes in the intensities of both currents in Figure 6d during this time despite their large amplitude.

Movie S1 provides a more extended two-dimensional view of the westward movement and varying intensity of several auroral regions during the interval shown.

In summary, this event occurred under moderately quiet geomagnetic conditions when satellite UV images showed isolated brighter auroral regions between Labrador and southern Greenland in an otherwise weak auroral oval. A significant brightening near and above Nain, on the east coast of Labrador, resulted in two intervals of large amplitude magnetic perturbations there, the first with derivative amplitudes exceeding 6 nT/s in all three components. SECS maps using magnetometer data from all available stations in this region showed that during both GMD intervals a pair of closely spaced downward and upward vertical currents (a proxy for field-aligned currents) was located on opposite sides of Nain, and a locally strengthened horizontal electrojet current perpendicular to their axis (example shown in Figure 5) was located above Nain.

3.2. Event 2: 20 April 2002 01:56–02:01 UT

During this event large amplitude (>16 nT/s) GMDs were observed at Gillam at 01:56 UT, at Fort Churchill 01:55-01:57 UT, and Coral Harbor (CHB) at 02:01 UT, during an interval of disturbed magnetospheric conditions. As shown in Movie S2, a bright auroral arc moved poleward after 01:50 UT, reached Gillam and Fort Churchill near the southwest coast of Hudson Bay by 1:56 UT, came very near to Coral Harbor, located near the northern end of Hudson Bay, between 02:00 UT and 02:02 UT, and gradually faded away after 02:06 UT.

This interval fell during the recovery phase of the first part of a two-stage magnetic storm that began near 09:00 UT on 19 April 2002 (not shown). The first main phase had two −132 nT minima in SYM/H at 18:58 UT and 21:40 UT on 19 April. This was followed by a complex recovery phase until ∼0400 UT on 20 April, when the shorter second main phase began; the SYM/H index fell to a −185 nT minimum at 06:01 UT on 20 April.

Figure 7 presents the more immediate context of this event, showing OMNI IMF and solar wind data and the SML, SMU, and SYM/H magnetic activity indices from 00:00 UT to 04:00 UT on this day. The IMF (panels a–c) showed considerable variability throughout this interval, but the solar wind velocity (panel d) exceeded 540 km/s throughout. A rapid magnetic field reorientation between 00:45 UT and 00:50 UT (panels a–c), during which the B_z component moved rapidly southward from +15 to −20 nT, coincided with a temporary decrease in V_{sw} (panel d), a temporary increase in P_{sw} (panel e), and a short-lived rise and fall in the SYM/H index (panel h). These changes were soon followed by a gradual and large decrease in the SML index (panel f) and a sharp rise in the SMU index (panel g) near 0100 UT. Strong auroral activity was indicated in panel f by SML values near −1,300 nT before 01:50 UT (the beginning of the shaded region in Figure 6), then rising briefly to −1,000 nT by 01:55 UT, and dropping rapidly to −1,600 at 02:05 UT. During this shorter interval, V_{sw} (panel d) was near 565 km/s, P_{sw} (panel e) was near 5 nPa, and IMF B_z (panel c) rose from −10 to −5 nT, but remained negative.

Table 3 lists the substorm onsets between 00:00 UT and 04:00 UT on 20 April 2002 identified in the five substorm lists. The onset at 00:25 UT did not match any significant change in the SML index, but the onset at 00:58 UT was consistent with the beginning of the gradual and large decrease in the SML index. The 01:18 UT onset, located at 11°E longitude in Scandinavia in the Newell and Gjerloev list, occurred shortly before a more rapid but short-lived SML decrease. The location of the 01:38 UT onset was placed at 353°E longitude (Faeroes, N of Scotland) in the Newell and Gjerloev list, but again no location for the 01:49 UT onset was supplied in the Chu et al. list. The 01:38 UT and 01:49 UT onsets coincided with minor fluctuations in SML, but no onset was evident in

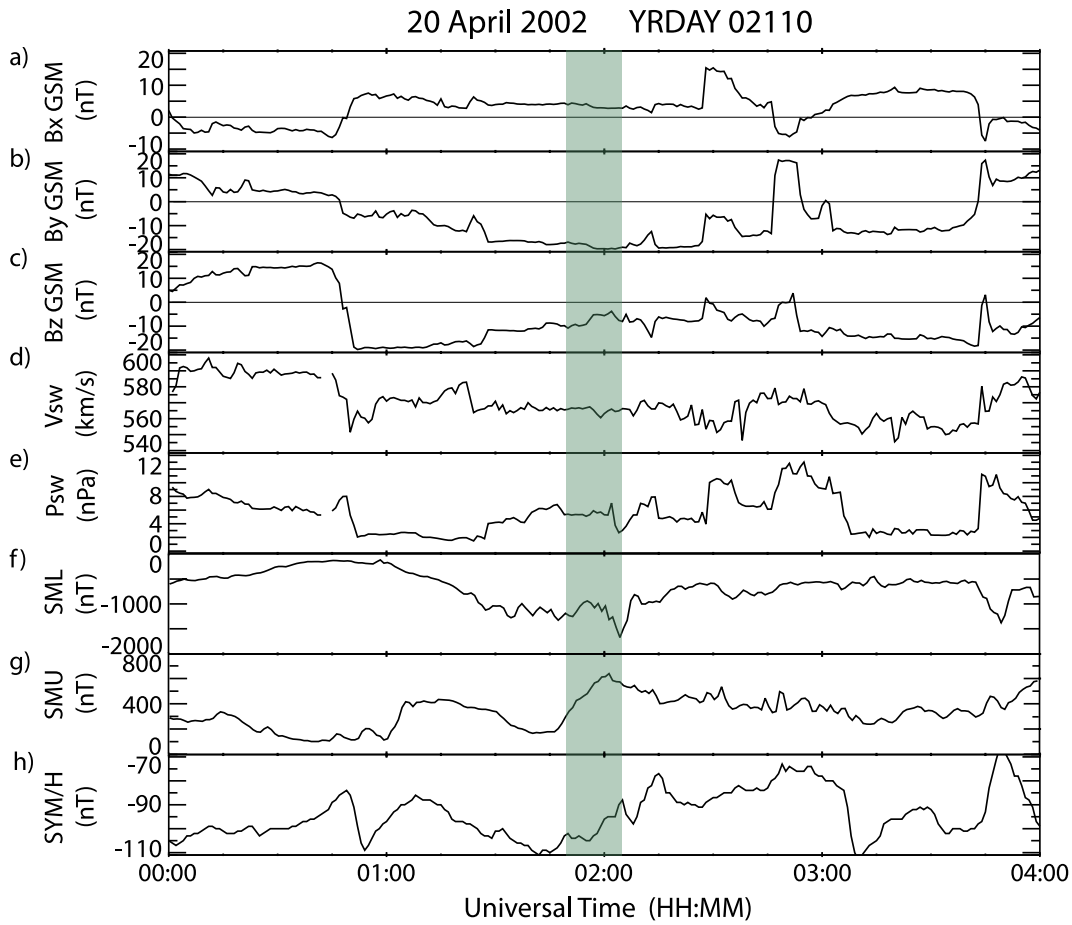

Figure 7. Time-shifted OMNI IMF and solar wind data (panels a–e) and the SML, SMU, and SYM/H magnetic activity indices (panels f–h) from 00:00 universal time (UT) to 04:00 UT 20 April 2002. The interval between 01:50 UT and 02:05 UT is shaded in green.

Table 3
Substorm Onsets Between 00:00 Universal Time (UT) and 04:00 UT on 20 April 2002, as Shown in Table 2

	Time (UT)	Onset location
Newell and Gjerloev	00:58	(Scandinavia 25°E)
	01:18	(Scandinavia 11°E)
	01:38	(Faeroes 353°E)
	02:30	(Greenland 310°E)
	03:14	(Scandinavia 21°E)
	03:42	(Scandinavia 11°E)
Forsyth et al.	02:30	(Scandinavia 21°E)
Frey et al.	03:38	(Quebec 287°E)
Ohtani and Gjerloev	None	
Chu et al.	00:25	No information
Chu et al.	01:49	No information
Chu et al.	03:07	No information

SML at either time. The Forsyth et al. and Newell and Gjerloev lists included onsets at 02:30 UT, some tens of minutes after the GMD events, but no onsets were recorded between 02:30 UT and 03:00 UT in any of the lists. Substorm onsets appeared after 03:00 UT in the Chu et al., Newell and Gjerloev, and Frey et al. lists, but it is notable that the Frey et al. list, based on IMAGE data, contained no onset until 03:38 UT. Movie S2, which shows successive FUV images from 00:05 UT to 03:59 UT, again provides a wide spatial and temporal context for this event.

Is it possible that a westward surge from the 01:38 UT onset could have propagated westward to this region to cause the negative bays? Movie S2 file shows that there was very little auroral activity over the Atlantic Ocean between 01:38 UT and 01:55 UT; the only significant activity was to the south and west of Hudson Bay. At 01:45:58, a 120 counts/pixel region appeared at the southern edge of Quebec, but it had faded to background levels by the time of the next image, perhaps indicating a pseudobreakup. However, at 01:48:01 UT, a sudden brightening of 250 counts/pixel appeared south of Hudson Bay (perhaps consistent with the onset in the Chu et al. list at 01:49 UT). It was followed by a rapid expansion and poleward movement toward Gillam by 01:54 UT, consistent with the onset of a weak substorm and its poleward expansion.

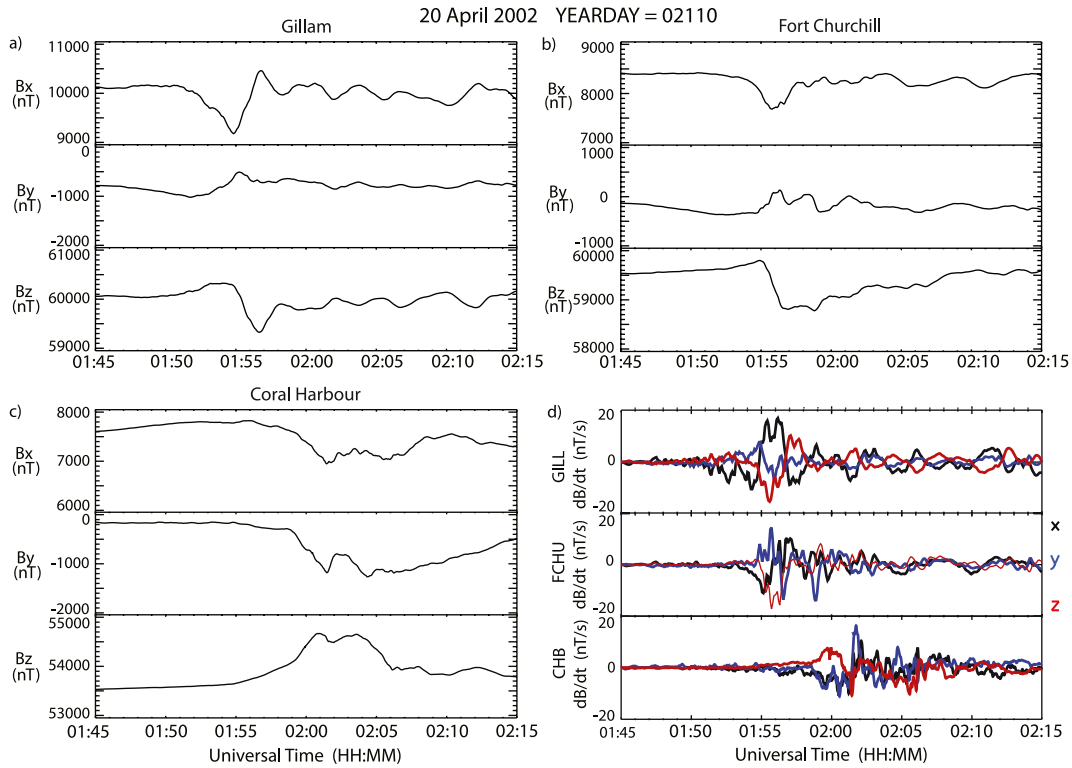

Figure 8. Magnetic field observations from (a) Gillam, (b) Fort Churchill, and (c) Coral Harbor from 01:45 universal time (UT) to 02:15 UT on 20 April 2000. The first three panels show the B_x, B_y, and B_z components in local magnetic coordinates. Panel d shows the color-coded derivatives of each component at each station.

We note that McPherron and Chu (2018) compared the Chu et al. and Forsyth et al. lists to several other onset lists, and found both significant differences in their waiting time distributions and relatively low levels of association between events. More recently, Lao et al. (2024) compared the contents of these and other lists of substorm onsets between 18 May 2000 and 31 December 2002, and concluded that although some degree of pairwise association was found between the lists, even lists generated by applying conceptually similar gradient-based identification to ground magnetometer data achieved an association with less than 50% event coincidence. The variety of onset lists reflects the complexity of substorm phenomena, so that although unambiguous identification of substorms and their onsets remains a challenge, these lists provide an important resource for evidence of significant magnetosphere- ionosphere activity.

Figure 8 presents three-axis magnetic field observations and color-coded derivatives of each component from Gillam, Fort Churchill, and Coral Harbor, from 01:45 UT to 02:15 UT on 20 April 2000. The magnetic field components at both Gillam (panel a) and 275 km to the north-northeast at Fort Churchill (panel b) were nearly constant from 00:50 UT to 01:50 UT (not shown), but rapid large excursions in all three components at these two stations that were simultaneous to within 2 min began and reached their first extrema near 01:50 UT and 01:55 UT, respectively. The changes in polarity at the two stations were similar in the B_y (up/down) and B_z (up/rapidly down/up) components, but the B_x component at Gillam exhibited large down/rapidly up/down variations, while at Fort Churchill the variations were down/up and smaller. Despite these differences in component directions, their derivatives at these two locations, shown in panel d, showed the largest peaks (17 nT/s = 1,020 nT/min) between 01:55 UT and 01:57 UT, but they differed considerably in the polarity of their components. A secondary peak appeared in B_y and B_x at 01:58 UT again in different components. Excursions in all three components began gradually at Coral Harbor, 833 km northeast of Fort Churchill, near 01:55 UT (panel c), and their extrema occurred between 02:01 UT and 02:03 UT. Peak derivatives at Coral Harbor (up to 16 nT/s) coincided in time with smaller but more rapid variations in B near 02:02 UT (panel c), but variations up to 8 nT/s occurred from 01:59 UT to 02:06 UT. Figure S2 in Supporting Information S1 shows the full daily magnetogram from Coral

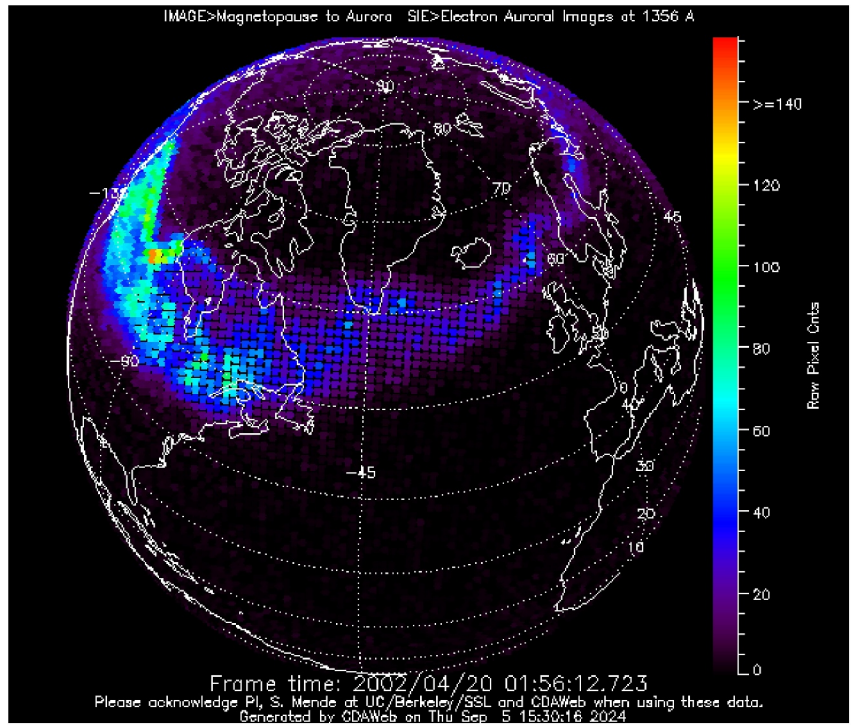

Figure 9. 1,356 Å auroral image from the IMAGE far ultraviolet Spectrographic Imager camera at 01:56:12.723 universal time, 20 April 2002.

Harbor, and Table S2 in Supporting Information S1 contains the times and amplitudes of all three magnetic field components at Gillam, Fort Churchill, and Coral Harbor near the time of their GMD maxima.

Figure 9 shows an FUV satellite image of the aurora at 01:56:13 UT, the time when the brightest and most extensive aurora was observed above Gillam and Fort Churchill and near the same time as the largest GMDs observed at both of these stations. A region with more than 140 counts per pixel appeared southwest of Gillam, and the region above these two stations had ~90 counts/pixel. Weak to moderate aurora appeared over much of central and eastern Canada, but only faint aurora appeared from eastern Labrador through Scandinavia and eastward into Siberia.

Figure 10, in a format similar to Figure 6, shows a keogram (panel a) and an ewogram (panel b) of the auroral intensity between 01:45 UT and 02:15 UT on 20 April 2002 observed between 50 and 80° MLat and in a range of ±7.5° MLon centered at −27.6°, the midpoint between the −27.4° MLon of FCHU and the −28.8° MLon of GILL. Panels c and d, copied from Figure 8d, show the color-coded derivatives of each component of the magnetic field at FCHU and GILL. Panels e and f are keograms and ewograms of the amplitude of SECS-derived vertical (upward and downward) currents. Both keograms are calculated within ±7.5° around −27.6°, the MLon of both FCHU and GILL.

Figure 10a shows that auroral precipitation (panel a) moved rapidly northward between 01:45 UT and 02:03 UT, and was most intense between 01:45 UT and 01:54 UT, by which time it had not yet reached 65°. The derivative amplitude at GILL (Figure 10c) began increasing near 01:51 UT, and at FCHU (Figure 10d) it began increasing 2 min later, near 01:53 UT. This progression is consistent with the higher MLat of FCHU than of GILL (but their identical MLon) and with the decrease with time of their distance to the northern edge of the auroral region.

The auroral precipitation was outside the narrow latitude range of Figure 10b until 01:54 UT, after which time it can be seen to have moved westward (toward more negative MLon) until after 02:10 UT. The region of increased auroral precipitation thus moved both northward and westward between 01:54 UT and 01:58 UT, reaching and moving slightly beyond the locations of FCHU and GILL. The derivative amplitudes at both FCHU and GILL peaked (Figure 10c) during the ~2 min interval centered at the time of the 01:56:13 image.

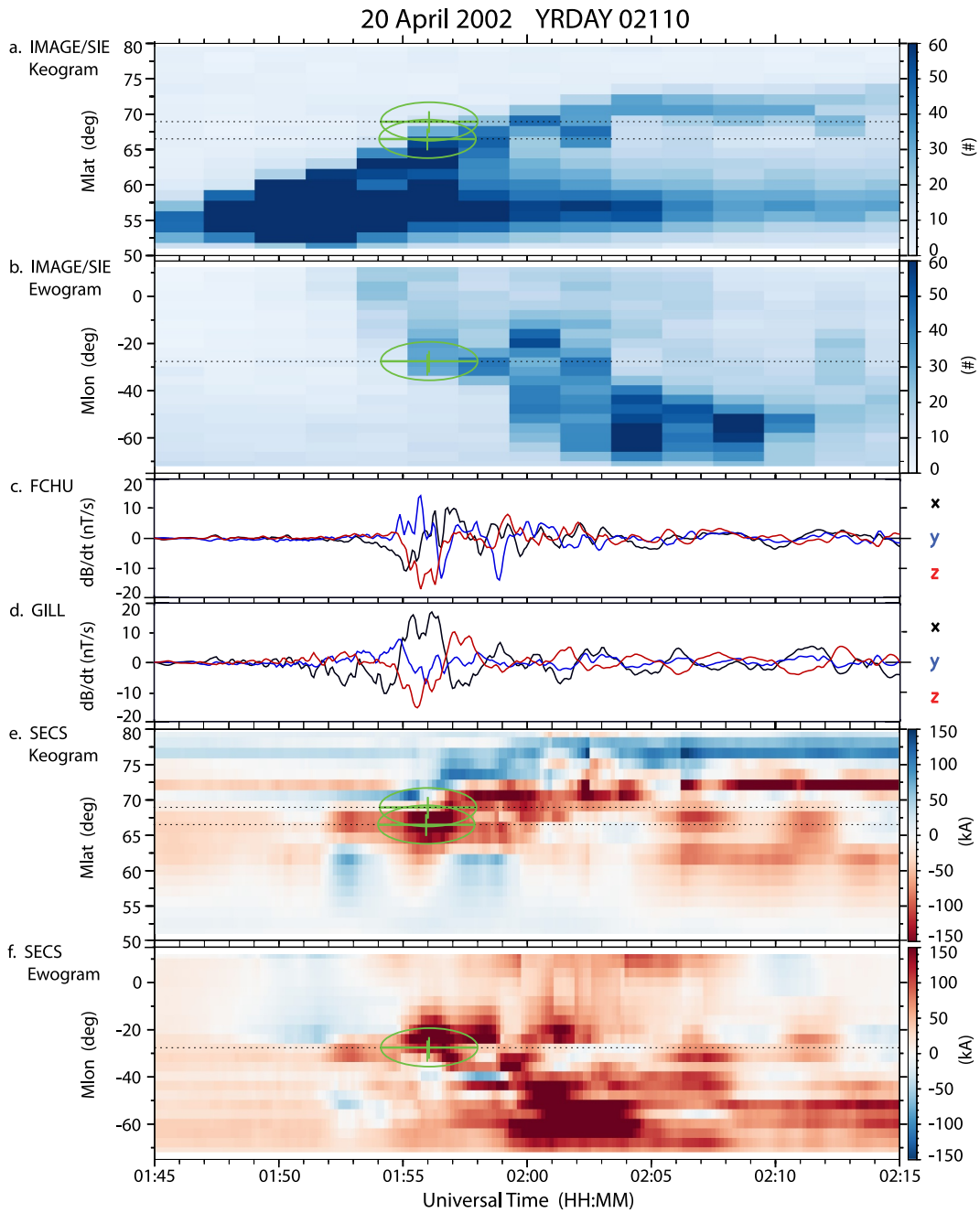

Figure 10. Panels (a) and (b) are keograms and ewograms of auroral intensity observed by the IMAGE SIE instrument between 01:45 universal time (UT) and 02:15 UT on 20 April 2002. Panels (c) and (d), copied from Figure 8d, show the color-coded derivatives of each component of the magnetic field at FCHU and GILL. Panels (e) and (f) are keograms and ewograms of the amplitude of SECS-derived vertical (upward and downward) currents. Both keograms (panels a and d) are calculated within ±7.5° around the −27.6° MLon of both FCHU and GILL, and the dashed lines show the 68.8° and 66.5° corrected magnetic latitudes of FCHU and GILL, respectively (vertical scale). Both ewograms (panels b and f) are calculated within ±2.5° around the 66.7° average MLAT value of these two stations, and the dashed lines show the −27.6° corrected magnetic longitude midpoint between the MLon values of −27.4° and −27.8° at FCHU and GILL, respectively (vertical scale). In panels (a), (b), (e), and (f), the green oval and cross hairs indicate the time of the peak *dB*/dt value shown in panels c and d (horizontal scale).

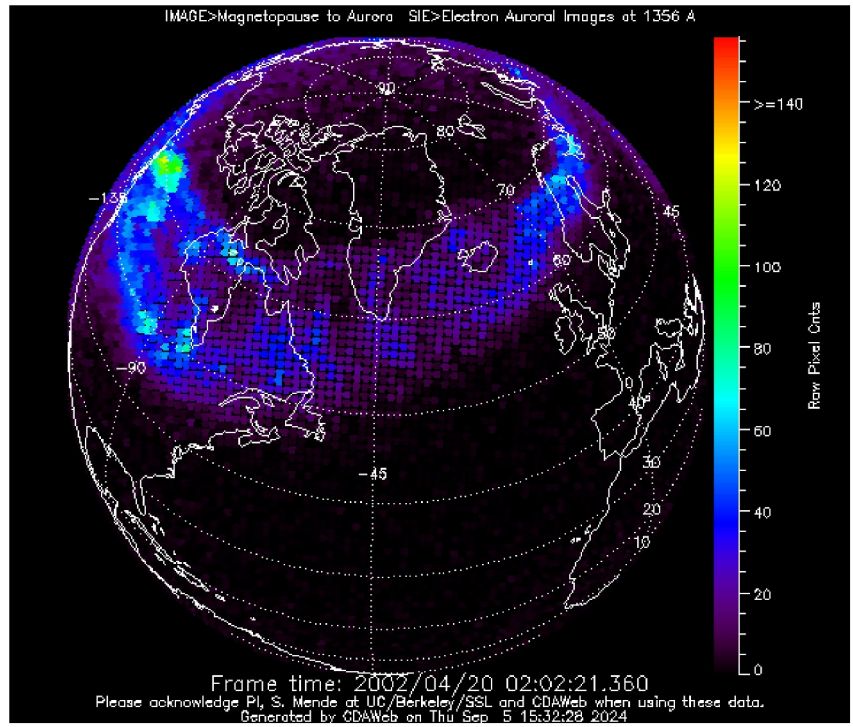

Figure 11. 1,356 Å auroral image from the IMAGE far ultraviolet Spectrographic Imager camera at 02:02:21.360 universal time, 20 April 2002.

The auroral intensity diminished slightly after 01:59 UT and bifurcated, with the northern part of the aurora continuing poleward, but after 02:02 UT the aurora exhibited neither rapid poleward motion nor significant changes in intensity. However, it continued to move westward away from both stations.

Figure 10e shows that between 01:55 UT and 01:57 UT the most intense upward currents were located above GILL and just south of FCHU, and Figure 10f shows that they were located overhead and just to the east of these stations, the same time interval with the strongest dB/dt at both stations.

A latitudinally localized region of downward currents appeared ∼2° poleward of the northern edge of the upward currents during this same interval. Latitudinally localized upward and downward currents shifted ∼3° poleward abruptly near 01:57 UT and remained there for 2 minutes before showing evidence of continued poleward motion until 02:02 UT, consistent with the poleward motion of the northern edge of the auroral region. During this interval, the vertical currents most clearly showed temporal variability down to 10-s scales (the cadence of the SECS maps) that cannot be identified using the auroral images (with ∼2 min cadence).

Somewhat weaker derivatives continued to appear at both stations between 01:58 UT and 02:02 UT, and more intermittently between 02:05 UT and 02:13 UT. During these intervals, the vertical currents were both somewhat weaker and not as close to the stations in either MLat or MLon.

Figure 11 shows an FUV satellite image of the aurora at 02:02:21 UT, the time when auroral power was observed slightly south of CHB, and shortly after the time of the largest GMD observed at that station, ∼02:01:45 UT. Four spatially limited regions with intensities between ∼60 and ∼110 counts per pixel appeared south of CHB, but nearby regions in all directions had intensities of ≤∼50 counts/pixel. More intense aurorae appeared only over central Canada far to the west and south.

Figure 12 covers the same time range as in Figure 10 and has a similar format but focuses on the activity observed near Coral Harbor. Panels a and b show the auroral intensity between 01:45 UT and 02:15 UT on 20 April 2002 observed between 50° and 80° MLat and in a range of ±7.5° MLon centered at the MLon value of Coral Harbor, −9.9°. Panel c repeats the color-coded derivative plot of Coral Harbor dB/dt in Figure 9d. Panels

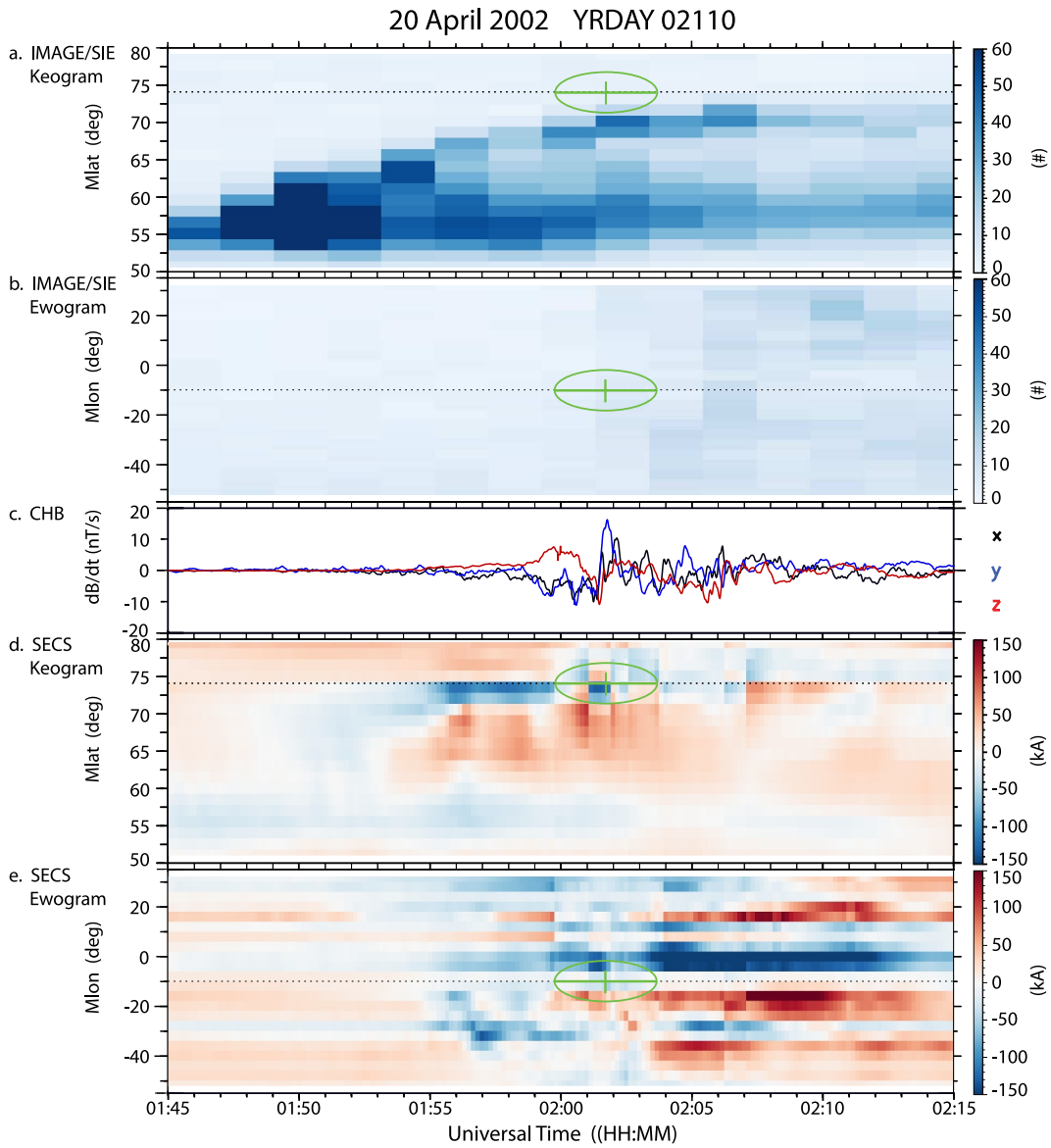

Figure 12. Panels (a) and (b) are keograms and ewograms of auroral intensity observed by the IMAGE SIE instrument between 01:45 universal time (UT) and 02:15 UT on 20 April 2002. Panel (c), copied from Figure 8d, shows the color-coded derivatives of each component of the magnetic field at Coral Harbor (CHB). Panels (d) and (e) are keograms and ewograms of the amplitude of Spherical Elementary Currents Systems-derived vertical (upward and downward) currents. Both keograms (panels a and d) are calculated within ±7.5° around the −9.9° MLon of CHB, and the dashed lines show the 74.1° corrected magnetic latitude of CHB (vertical scale). Both ewograms (panels b and e) are calculated within ±2.5° around the 74.1° MLat of CHB, and the dashed lines show the −9.9° corrected magnetic longitude of CHB (vertical scale). In panels (a), (b), (d), and (e) the green oval and cross hairs indicate the time of the peak *dB/dt* value shown in panel (c) (horizontal scale).

d and e show the amplitude of SECS-derived vertical (upward and downward) currents observed between 30° and 50° MLon and in a range of ±2.5° centered at the MLat value of Coral Harbor, 74.1°.

The northward progressions of the aurora and its amplitude variations in both time and space in this MLon sector (Figure 12a) are similar to those in Figure 11a, although the amplitudes were slightly weaker. At 02:02:21 UT, shortly after the time of the peak dB/dt (Figure 12c), the poleward edge of the auroral region neared the location of the magnetometer station (CHB) but did not extend over it. Thus, in both Figures 11 and 12, the peak GMD occurred near the poleward edge of the auroral region as it was moving poleward—above GILL but only coming

near to FCHU or CHB. Figure 12b is nearly featureless, indicating that only very weak aurora appeared within ±2.5° of the MLat of CHB over a wide range of MLon until after 02:03 UT.

Figure 12d shows that the interval from 01:55 UT to 01:59:40 UT, during which dB/dt was generally increasing, was characterized by downward currents extending ∼3° south from the MLat of CHB and upward currents extending both 5° or more farther to the south and from 2° to 5° north of CHB, most exhibiting modest temporal variations. Beginning at 01:59:40 UT, the downward currents south of CHB suddenly disappeared and upward currents between 68° and 73° MLat (south of CHB) gradually intensified, as also did downward currents between 74° and 79° MLT (north of CHB). Between 02:01 UT and 02:01:50 UT, a strong downward current suddenly appeared adjacent to and immediately south of CHB and a somewhat weaker upward current suddenly appeared immediately to the north. These currents near CHB suddenly disappeared again at 02:01:50 UT, the time of the peak GMD (Figure 12c), and moderately strong currents suddenly reappeared, downward north of CHB and upward from 2° to ∼10° south of CHB. These currents continued through 02:15 UT, but with numerous temporal variations, as did also the somewhat weaker derivatives.

Figure 12e, which shows currents only within ±2.5° MLat of CHB, shows that only very weak vertical currents of either sign appeared within ±4° MLon of CHB. Only between 02:01 UT and 02:01:50 UT did a weak downward current region appear within ±4° MLon of CHB; during this interval a strong downward current also appeared immediately south of CHB (as shown in Figure 12d), as also did the peak GMD. Both downward and upward currents appeared nearly continuously between 02:03 UT and 02:15 UT at distances between 4 and 12 MLon either side of CHB, but only between 02:04 UT and 02:07 UT, when upward currents showed considerable temporal variability, did the derivative amplitudes again reach 10 nT/s.

In summary, this event occurred during the recovery phase of a strong magnetic storm, when satellite UV images showed the poleward movement of a much brighter auroral region over the west coast of Hudson Bay and the subsequent movement of a weaker auroral arc to the northern edge of Hudson Bay. The successive passage of this auroral region over GILL and FCHU produced intense GMDs (>16 nT/s) at both stations at 01:56 UT and a slightly weaker GMD at FCHU 2 min later.

The northern edge of the aurora continued to move poleward and extended to just south of CHB before becoming stationary near 02:02 UT. Observations at Coral Harbor showed ∼10 min of increased GMD amplitudes between 01:59 UT and 02:09 UT: a 6 nT/s peak in B_z near 02:00 UT, a 16 nT/s peak in B_y and an 11 nT/s peak in B_x between 02:01:30 and 02:02:00 UT, and an additional 10 nT/s peak in B_x and B_z between 02:05 UT and 02:06:30 UT. The upward and downward current regions moved only slightly between 02:00 UT and 02:07 UT, but the most intense downward current occurred immediately south of CHB and slightly to the east between 02:01 UT and 02:01:50 UT, at the same time as the largest GMD.

4. Discussion

We have presented two intervals of successive large-scale images of Earth's aurora obtained by the far ultraviolet (FUV) Spectrographic Imager (SI) camera on the IMAGE satellite that showed auroral enhancements closely associated with large GMDs observed in ground-based magnetometer data. Event 1 occurred during quiet conditions unrelated to either a magnetic storm or a substorm. Event 2 occurred during the still-disturbed recovery phase of a moderate storm. Its association with the poleward expansion of a discrete auroral arc is similar to the events observed during two magnetic storms described by Ngwira et al. (2018). The Frey et al. list, based on IMAGE observations, included no substorm onset during this event, and no onsets in the North American sector were included in the Forsyth et al. Newell and Gjerloev lists. However, the Chu et al. list, which does not provide location information, included an onset ∼7 min before the appearance of large GMDs at GILL and FCHU, although the Frey et al. list did not include it. It is thus possible but not certain that event 2 was associated with a substorm.

Large values of dB/dt at individual magnetometer sites correlated closely with overhead auroras as well as with nearby temporally varying vertical up-down current pairs. The proximity of such current pairs and locally intensified perpendicular electrojet currents to the location of a strong GMD is common to many recent studies of premidnight GMDs (Engebretson, Steinmetz, et al., 2019; Engebretson, Gaffaney, et al., 2024; McCuen et al., 2023; Ngwira et al., 2015, 2018, 2023, 2025; Shi et al., 2025; Weygand et al., 2021).

A recent study by Walker et al. (2024) provides evidence that strong local enhancements of ionospheric conductance, produced by the localized vertical currents associated with these GMDs, can change the ground magnetic field and in particular the westward electrojet. The localized rotation of the northwestward electrojets shown in the SECS image for event 1 at 23:16:20 UT on 22 December 2000 (Figure 5) is an additional example of such a localized effect.

Event 1 shows a rapid westward movement of a bright auroral region over Nain from 23:13:39 UT to 23:17:44 UT on 22 December 2000 (Figure 6), and event 2 shows rapid poleward movements of an auroral arc over GILL and FCHU from 01:52:07 UT to 01:58:16 UT (Figure 10) and a similar poleward movement to near CHB from 01:45 UT to 02:03 UT (Figure 12), both on 20 April 2002. The rapid auroral movements captured in these global images suggest the possibility that the motion of horizontal currents as well as temporal changes in their intensity may cause the observed magnetic variations, as suggested by Apatenkov et al. (2020). This study noted that the value of the total time derivative of dB/dt observed on the ground is $dB/dt = \partial B/\partial t + (\mathrm{V} \cdot \nabla)B$. It may be an interesting topic for future work using a numerical simulation validated with the IMAGE and ground magnetometer data to calculate each part of this derivative separately.

It is important to stress that images of the aurora from high altitude spacecraft can ideally serve as supplements to ground-based imagers, serving as replacements for them only when no ground-based imager data are available. Many ground-based auroral imagers have been deployed in the past two decades, including the white-light THEMIS all-sky imagers (Donovan et al., 2006; Mende et al., 2008), 2004-present, and Redline Geospace Observatory (REGO) imagers (Donovan, 2014), 2014-present, both in Arctic Canada. These high-cadence imager arrays have contributed to substantial increases in the detailed understanding of auroral and ionospheric processes, but they cannot provide global views of the aurora; their coverage cannot extend over oceans or remote locations on the ground that are distant from sources of electrical power. Conversely, the cadence of a high-altitude satellite imager such as the soon to be launched SMILE mission (Branduardi-Raymont et al., 2018) is limited to one UVI image per minute, and its highly elliptical polar orbit with 51-hr period will provide extended but not complete temporal coverage over the northern polar regions. Ground-based imagers can also sample more rapidly than space-based imagers for several reasons, including ease of data transfer and proximity to light source, enabling shorter exposure times.

We expect that the combination of global images from high altitude spacecraft such as SMILE and the growing number of high sampling rate ground-based imagers, including the SMILE ASI network of color imagers that are beginning to replace the THEMIS imagers as of 2024 (Carter et al., 2024), will provide even more comprehensive observational support for studies of the physics of a wide variety of both large-scale and mesoscale processes involved in magnetosphere-ionosphere coupling.

5. Conclusions

We found that regions of large dB/dt and SECS maps of localized up/down vertical currents and equivalent ionospheric currents that previous studies have shown to coincide with temporally and/or spatially localized auroral motions or intensifications visible in data obtained by ground-based auroral imagers can also be identified in high-altitude FUV satellite images. As a result, auroral images obtained by future high-altitude spacecraft are likely to be able to not only provide large-spatial-scale context for a range of mesoscale phenomena, including large dB/dt that can generate large GICs in susceptible infrastructure, but also provide information on GMDs that occur in locations distant from existing ground-based imagers. We have also shown that these mesoscale phenomena can appear or disappear in a few tens of seconds, so imaging at a high cadence will be necessary in order to resolve them.

It is not yet possible to predict where or when individual GMDs will occur using either magnetometer or imager data. Because the highly localized GMDs in the premidnight sector have only recently been confirmed to be linked to mesoscale dipolarizing flux bundles (components of bursty bulk flows) observed in the near magnetotail (Engebretson, Gaffaney, et al., 2024; Ngwira et al., 2025; Runov et al., 2025), which are in turn generated by localized reconnection deeper in the tail, the ability to predict their occurrence and location rather than simply nowcast it will depend on further advances in both observing and modeling the occurrence and location of such reconnection activity. We suspect that such advances may need to include finer spatially detailed information about the near-Earth solar wind and IMF and their interaction with the entire magnetosphere.

Data Availability Statement

Ground-based magnetometer data used in this study were recorded at stations in the MACCS (Engebretson et al., 2011) and CARISMA (Mann et al., 2023) arrays in Eastern Arctic Canada. Time-shifted solar wind and interplanetary magnetic field data from the OMNI database and data from the Far Ultraviolet Imager on the IMAGE spacecraft are available at https://cdaweb.gsfc.nasa.gov/. SECS maps at a 1-min cadence are available at http://vmo.igpp.ucla.edu/data1/SECS/Quicklook/; higher time resolution maps are available on demand from James Weygand. The SuperMAG SML and SMU indices and substorm lists accessed in this study are available from the SuperMAG web site (Gjerloev, 2012, 2023).

Acknowledgments
This research was supported by National Science Foundation Grants AGS-2013648 to Augsburg University and AGS-2013433 to the University of Michigan. Work by JMW was supported by NASA Grants HSR-80NSSC18K1227 and SWO2R 80NSSC20K1364, NASA contract HPDE-80GSFC17C0018, NSF Grants GEO-NERC 2027190, GEM-2400140, and NSF Grant AGS-2013648 via subcontract from Augsburg University. Work by MDH was supported by NASA Grant 80NSSC19K0907 and NSF Grant AGS-2027210. Work by CMN was supported by NASA Grant HSR-80NSSC24K0259 and NSF Grant AGS-2300579. We thank Ian Mann, D. K. Milling, A. Kale and the rest of the CARISMA team for data. CARISMA is operated by the University of Alberta and funded by the Canadian Space Agency. We gratefully acknowledge the SuperMAG collaborators (https://supermag.jhuapl.edu/info/?page=acknowledgement).

References

Amm, O. (1997). Ionospheric elementary current systems in spherical coordinates and their application. *Journal of Geomagnetism and Geoelectricity*, *49*(7), 947–955. https://doi.org/10.5636/jgg.49.947

Amm, O., Engebretson, M. J., Hughes, T., Newitt, L., Viljanen, A., & Watermann, J. (2002). A traveling convection vortex event study: Instantaneous ionospheric equivalent currents, estimation of field-aligned currents, and the role of induced currents. *Journal of Geophysical Research*, *107*(A11), SIA1-1–SIA1-11. https://doi.org/10.1029/2002JA009472

Amm, O., & Viljanen, A. (1999). Ionospheric disturbance magnetic field continuation from the ground to the ionosphere using spherical elementary currents systems. *Earth Planets and Space*, *51*(6), 431–440. https://doi.org/10.1186/BF03352247

Anderson, B. J., Korth, H., Waters, C. L., Green, D. L., & Stauning, P. (2008). Statistical Birkeland current distributions from magnetic field observations by the Iridium constellation. *Annales Geophysicae*, *26*(3), 671–687. https://doi.org/10.5194/angeo-26-671-2008

Apatenkov, S. V., Pilipenko, V. A., Gordeev, E. I., Viljanen, A., Juusola, L., Belakhovsky, V. B., et al. (2020). Auroral omega bands are a significant cause of large geomagnetically induced currents. *Geophysical Research Letters*, *47*(6), e2019GL086677. https://doi.org/10.1029/2019GL086677

Boteler, D. H. (2019). A 21st century view of the March 1989 magnetic storm. *Space Weather*, *17*(10), 1427–1441. https://doi.org/10.1029/2019SW002278

Boteler, D. H., Pirjola, R. J., & Nevanlinna, H. (1998). The effects of geomagnetic disturbances on electrical systems at the Earth's surface. *Advances in Space Research*, *22*(1), 17–27. https://doi.org/10.1016/S0273-1177(97)01096-X

Branduardi-Raymont, G., Wang, C., Escoubet, C. P., Adamovic, M., Agnolon, D., Berthomier, M., et al. (2018). SMILE definition study report, European Space Agency, ESA/SCI, 1. https://doi.org/10.5270/esa.smile.definition_study_report-2018-12

Burch, J. (2000). IMAGE mission overview. *Space Science Reviews*, *91*(1/2), 1–14. https://doi.org/10.1023/A:1005245323115

Carrington, R. C. (1859). Description of a singular appearance seen in the Sun on September 1, 1859. *Monthly Notices of the Royal Astronomical Society*, *20*(1), 13–15. https://doi.org/10.1093/mnras/20.1.13

Carter, J. A., Dunlop, M., Forsyth, C., Oksavik, K., Donovon, E., Kavanagh, A., et al. (2024). Ground-based and additional science support for SMILE. *Earth and Planetary Sciences*, *8*, 275–298. https://doi.org/10.26464/epp2023055

Chu, X., McPherron, R. L., Hsu, T.-S., & Angelopoulos, V. (2015). Solar cycle dependence of substorm occurrence and duration: Implications for onset. *Journal of Geophysical Research*, *120*(4), 2808–2818. https://doi.org/10.1002/2015JA021104

Donovan, E. (2014). REGO all sky imager data [Dataset]. *University of Calgary, Canada*. https://data.phys.ucalgary.ca/sort_by_instrument/all_sky_camera/GO-Canada_REGO/stream0

Donovan, E., Mende, S. B., Jackel, B., Frey, H. U., Syrjasuo, M., Voronkov, I., et al. (2006). The THEMIS all-sky imaging array—System design and initial results from the prototype imager. *Journal of Atmospheric and Solar-Terrestrial Physics*, *68*(13), 1472–1487. https://doi.org/10.1016/j.jastp.2005.03.027

Engebretson, M. J., Gaffaney, S. A., Ochoa, J. A., Runov, A., Weygand, J. M., Nishimura, Y., et al. (2024). Signatures of dipolarizing flux bundles in the nightside auroral zone. *Journal of Geophysical Research: Space Physics*, *129*(4), e2023JA032266. https://doi.org/10.1029/2023JA032266

Engebretson, M. J., Hughes, W. J., Alford, J. L., Zesta, E., Cahill, L. J., Jr., Arnoldy, R. L., & Reeves, G. D. (1995). Magnetometer array for cusp and cleft studies observations of the spatial extent of broadband ULF magnetic pulsations at cusp/cleft latitudes. *Journal of Geophysical Research*, *100*(A10), 19371–19386. https://doi.org/10.1029/95JA00768

Engebretson, M. J., Pilipenko, V. A., Ahmed, L. Y., Posch, J. L., Steinmetz, E. S., Moldwin, M. B., et al. (2019). Nighttime magnetic perturbation events observed in Arctic Canada: 1. Survey and statistical analysis. *Journal of Geophysical Research: Space Physics*, *124*(9), 7442–7458. https://doi.org/10.1029/2019JA026794

Engebretson, M. J., Steinmetz, E., & Moldwin, M. (2011). MACCS 0.5 s ground magnetometer data [Dataset]. *Augsburg University*. https://doi.org/10.48322/sydj-ab90

Engebretson, M. J., Steinmetz, E. S., Posch, J. L., Pilipenko, V. A., Moldwin, M. B., Connors, M. G., et al. (2019). Nighttime magnetic perturbation events observed in Arctic Canada: 2. Multiple-instrument observations. *Journal of Geophysical Research: Space Physics*, *124*(9), 7459–7476. https://doi.org/10.1029/2019JA026797

Engebretson, M. J., Yang, L., Steinmetz, E. S., Pilipenko, V. A., Moldwin, M. B., McCuen, B. A., et al. (2024). Extreme geomagnetic disturbances (GMDs) observed in Eastern Arctic Canada: Occurrence characteristics and solar cycle dependence. *Journal of Geophysical Research: Space Physics*, *129*(1), e2023JA031643. https://doi.org/10.1029/2023JA031643

Forsyth, C., Rae, I. J., Coxon, J. C., Freeman, M. P., Jackman, C. M., Gjerloev, J., & Fazakerley, A. N. (2015). A new technique for determining substorm onsets and phases from indices of the electrojet (SOPHIE). *Journal of Geophysical Research: Space Physics*, *120*(12), 10592–10606. https://doi.org/10.1002/2015JA021343

Frank, L. A., & Craven, J. D. (1988). Imaging results from Dynamics explorer 1. *Reviews of Geophysics*, *26*(2), 249–283. https://doi.org/10.1029/RG026i002p00249

Frey, H. U., & Mende, S. B. (2006). Substorm onsets as observed by IMAGE-FUV. *International Conference Substorms*, *8*, 71–75.

Frey, H. U., Mende, S. B., Angelopoulos, V., & Donovan, E. F. (2004). Substorm onset observations by IMAGE-FUV. *Journal of Geophysical Research*, *109*(A10), A10304. https://doi.org/10.1029/2004JA010607

Frey, H. U., Mende, S. B., Carlson, C. W., Gérard, J.-C., Hubert, B., Spann, J., et al. (2001). The electron and proton Aurora as seen by IMAGE-FUV and FAST. *Geophysical Research Letters*, *28*(6), 1135–1138. https://doi.org/10.1029/2000GL012352

Germany, G. A., Parks, G. K., Brittnacher, M., Cumnock, J., Lummerzheim, D., Spann, J. F., et al. (1997). Remote determination of auroral energy characteristics during substorm activity. *Geophysical Research Letters*, *24*(8), 995–998. https://doi.org/10.1029/97GL00864

Gjerloev, J. W. (2012). The SuperMAG data processing technique. *Journal of Geophysical Research*, *117*(A9), A09213. https://doi.org/10.1029/2012JA017683

Gjerloev, J. W. (2023). SuperMAG, global magnetic field observations and products made possible by the contributors [Dataset]. *Applied Physics Laboratory*. https://supermag.jhuapl.edu/

Hapgood, M. (2019). The great storm of May 1921: An exemplar of a dangerous space weather event. *Space Weather*, *17*(7), 950–975. https://doi.org/10.1029/2019SW002195

Hubert, B., Gerard, J.-C., Evans, D. S., Meurant, M., Mende, S. B., Frey, H. U., & Immel, T. J. (2002). Total electron and proton energy input during auroral substorms: Remote sensing with IMAGE-FUV. *Journal of Geophysical Research*, *107*(A8), 1183. https://doi.org/10.1029/2001JA009229

Immel, T. J., Mende, S. B., Frey, H. U., Patel, J., Bonnell, J. W., Engebretson, M. J., & Fuselier, S. A. (2005). ULF waves associated with enhanced subauroral proton precipitation. In J. Burch, M. Schulz, & H. Spence (Eds.), *Inner magnetosphere interactions: New perspectives from Imaging, geophysical monograph series 159* (pp. 71–84). American Geophysical Union. https://doi.org/10.1029/159GM05

Juusola, L., Nakamura, R., Amm, O., & Kauristie, K. (2009). Conjugate ionospheric equivalent currents during bursty bulk flows. *Journal of Geophysical Research*, *114*(A4), A04313. https://doi.org/10.1029/2008JA013908

Kappenman, J. G. (2001). Advanced geomagnetic storm forecasting for the electric power industry. In P. Song, H. Singer, & G. Siscoe (Eds.), *Space weather, geophysical monograph series, 125* (pp. 353–358). American Geophysical Union. https://doi.org/10.1029/GM125p0353

Kistler, L. M., Frey, H. U., Möbius, E., Mouikis, C., Quinn, J. M., Klecker, B., et al. (2002). Motion of auroral ion outflow structures observed with CLUSTER and IMAGE FUV. *Journal of Geophysical Research*, *107*(A8), 1186. https://doi.org/10.1029/2001JA005075

Lao, C. J., Forsyth, C., Freeman, M. P., Smith, A. W., & Mooney, M. K. (2024). On the association of substorm identification methods. *Journal of Geophysical Research: Space Physics*, *129*(9), e2024JA032762. https://doi.org/10.1029/2024JA032762

Love, J. J., Hayakawa, H., & Cliver, E. W. (2019). Intensity and impact of the New York railroad superstorm of May 1921. *Space Weather*, *17*(8), 1281–1292. https://doi.org/10.1029/2019SW002250

Mann, I. R., Milling, D. K., & Kale, A. (2023). CARISMA magnetometer network [Dataset]. *University of Alberta*. Retrieved from https://carisma.ca

Mann, I. R., Milling, D. K., Rae, I. J., Ozeke, L. G., Kale, A., Kale, Z. C., et al. (2008). The upgraded CARISMA magnetometer array in the THEMIS era. *Space Science Reviews*, *141*(1-4), 413–451. https://doi.org/10.1007/s11214-008-9457-6

Marklund, G. T., Blomberg, L. G., Potemra, T. A., Murphree, J. S., Rich, F. J., & Stasiewicz, K. (1987). A new method to derive "instantaneous" high-latitude potential distributions from satellite measurements including auroral imager data. *Geophysical Research Letters*, *14*(4), 439–442. https://doi.org/10.1029/GL014i004p00439

McCuen, B. A., Moldwin, M. B., Engebretson, M. J., Weygand, J. M., & Nishimura, Y. (2023). Magnetosphere-ionosphere drivers of transient-large amplitude geomagnetic disturbances: Statistical analysis and event study. *Journal of Geophysical Research: Space Physics*, *128*(11), e2023JA031587. https://doi.org/10.1029/2023JA031587

McPherron, R. L., & Chu, X. (2018). The midlatitude positive bay index and the statistics of substorm occurrence. *Journal of Geophysical Research: Space Physics*, *123*(4), 2831–2850. https://doi.org/10.1002/2017JA024766

McPherron, R. L., Hsu, T.-S., & Angelopoulos, V. (2015). Solar cycle dependence of substorm occurrence and duration: Implications for onset. *Journal of Geophysical Research: Space Physics*, *120*(4), 2808–2818. https://doi.org/10.1002/2015JA021104

Mende, S. B., Frey, H. U., Carlson, C. W., McFadden, J., Gérard, J.-C., Hubert, B., et al. (2002). IMAGE and FAST observations of substorm recovery phase aurora. *Geophysical Research Letters*, *29*(12), 43. https://doi.org/10.1029/2001GL013027

Mende, S. B., Harris, S. E., Frey, H. U., Angelopoulos, V., Russell, C. T., Donovan, E., et al. (2008). The THEMIS array of ground-based observatories for the study of auroral substorms. *Space Science Reviews*, *141*(1–4), 357–387. https://doi.org/10.1007/978-0-387-89820-9_16

Mende, S. B., Heetderks, H., Frey, H. U., Lampton, M., Geller, S. P., Habraken, S., et al. (2000). Far ultraviolet imaging from the IMAGE spacecraft. 1. System design. *Space Science Reviews*, *91*(1/2), 243–270. https://doi.org/10.1023/A:1005271728567

Mende, S. B., Heetderks, H., Frey, H. U., Stock, J. M., Lampton, M., Geller, S. P., et al. (2000). Far ultraviolet imaging from the IMAGE spacecraft. 3. Spectral imaging of Lyman-α and OI 135.6 nm. *Space Science Reviews*, *91*(1/2), 287–318. https://doi.org/10.1023/A:1005292301251

Milan, S. E., Imber, S. M., Fleetham, A. L., & Gjerloev, J. (2023). Solar cycle and solar wind dependence of the occurrence of large *dB/dt* events at high latitudes. *Journal of Geophysical Research: Space Physics*, *128*(4), e2022JA030953. https://doi.org/10.1029/2022JA030953

National Academies of Sciences, Engineering, and Medicine. (2024). *The next decade of discovery in solar and space physics: Exploring and safeguarding humanity's home in space*. The National Academies Press. https://doi.org/10.17226/27938

Newell, P. T., & Gjerloev, J. W. (2011). Evaluation of SuperMAG auroral electrojet indices as indicators of substorms and auroral power. *Journal of Geophysical Research*, *116*(A12), 12211. https://doi.org/10.1029/2011JA016779

Ngwira, C. M., Arritt, R., Perry, C., Weygand, J. M., & Sharma, R. (2023). Occurrence of large geomagnetically induced currents within the EPRI SUNBURST monitoring network. *Space Weather*, *21*(12), e2023SW003532. https://doi.org/10.1029/2023SW003532

Ngwira, C. M., Nishimura, Y., Weygand, J. M., Engebretson, M. J., Pulkkinen, A., & Schuck, P. W. (2025). Observations of localized horizontal geomagnetic field variations associated with a magnetospheric fast flow burst during a magnetotail reconnection event detected by the THEMIS spacecraft. *Journal of Geophysical Research: Space Physics*, *130*(1), e2024JA032651. https://doi.org/10.1029/2024JA032651

Ngwira, C. M., Pulkkinen, A., Bernabeu, E., Eichner, J., Viljanen, A., & Crowley, G. (2015). Characteristics of extreme geoelectric fields and their possible causes: Localized peak enhancements. *Geophysical Research Letters*, *42*(17), 6916–6921. https://doi.org/10.1002/2015GL065061

Ngwira, C. M., Sibeck, D., Silveria, M. V. D., Georgiou, M., Weygand, J. M., Nishimura, Y., & Hampton, D. (2018). A study of intense local dB/dt variations during two geomagnetic storms. *Space Weather*, *16*(6), 676–693. https://doi.org/10.1029/2018SW001911

Ohtani, S., & Gjerloev, J. W. (2020). Is the substorm current wedge an ensemble of wedgelets? Revisit to midlatitude positive bays. *Journal of Geophysical Research: Space Physics*, *125*(9), e2020JA027902. https://doi.org/10.1029/2020JA027902

Runov, A., Angelopoulos, V., Artemyev, A. V., Birn, J., Engebretson, M. J., Weygand, J. M., & Xu, Z. (2025). THEMIS observations of relativistic electrons at the nightside transition region during HILDCAA events. *Journal of Geophysical Research: Space Physics*, *130*(2), e2024JA033179. https://doi.org/10.1029/2024JA033179

Shi, X., Hartinger, M. D., Zou, Y., Rigler, E. J., Weygand, J. M., Kelbert, A., et al. (2025). Multi-scale intense geoelectric and geomagnetic field perturbations observed after an interplanetary magnetic field turning. *Space Weather*, *23*(2), e2024SW004046. https://doi.org/10.1029/2024SW004046

Vanhamäki, H., & Amm, O. (2011). Analysis of ionospheric electrodynamic parameters on mesoscales—A review of selected techniques using data from ground-based observation networks and satellites. *Annales Geophysicae*, *29*(3), 467–491. https://doi.org/10.5194/angeo-29-467-2011

Viljanen, A. (1997). The relation between geomagnetic variations and their time derivatives and implications for estimation of induction risks. *Geophysical Research Letters*, *24*(6), 631–634. https://doi.org/10.1029/97GL00538

Walker, S. J., Laundal, K. M., Reistad, J. P., Hatch, S. M., Ohma, A., & Gjerloev, J. (2024). The ionospheric leg of the substorm current wedge: Combining iridium and ground magnetometers. *Journal of Geophysical Research: Space Physics*, *129*(7), e2024JA032414. https://doi.org/10.1029/2024JA032414

Weygand, J. M. (2009a). *Equivalent ionospheric currents (EICs) derived using the spherical elementary current systems (SECS) technique at 10 s resolution in geographic coordinates*. University of California. https://doi.org/10.21978/P8D62B

Weygand, J. M. (2009b). Spherical elementary current (SEC) amplitudes derived using the spherical elementary currents systems (SECS) technique at 10 sec resolution in geographic coordinates. *UCLA*. https://doi.org/10.21978/P8PP8X

Weygand, J. M., Amm, O., Viljanen, A., Angelopoulos, V., Murr, D., Engebretson, M. J., et al. (2011). Application and validation of the spherical elementary currents systems technique for deriving ionospheric equivalent currents with the North American and Greenland ground magnetometer arrays. *Journal of Geophysical Research*, *116*(A3), A03305. https://doi.org/10.1029/2010JA016177

Weygand, J. M., Engebretson, M. J., Pilipenko, V. A., Steinmetz, E. S., Moldwin, M. B., Connors, M. G., et al. (2021). SECS analysis of nighttime magnetic perturbation events observed in Arctic Canada. *Journal of Geophysical Research: Space Physics*, *126*(11), e2021JA029839. https://doi.org/10.1029/2021JA029839

Weygand, J. M., Hartinger, M. D., Strangeway, R. J., Welling, D. T., Kim, H., Matzka, J., & Clauer, C. R. (2023). Interhemispheric asymmetry due to IMF by within the cusp spherical elementary currents. *Journal of Geophysical Research: Space Physics*, *128*(6), e2023JA031430. https://doi.org/10.1029/2023JA031430

Weygand, J. M., & Wing, S. (2016). Comparison of DMSP and SECS region-1 and region-2 ionospheric current boundary. *Journal of Atmospheric and Solar-Terrestrial Physics*, *143*, 8–13. https://doi.org/10.1016/j.jastp.2016.03.002

Zhang, Y., Paxton, L. J., Immel, T. J., Frey, H. U., & Mende, S. B. (2003). Sudden solar wind dynamic pressure enhancements and dayside detached auroras: IMAGE and DMSP observations. *Journal of Geophysical Research*, *108*(A4), 8001. https://doi.org/10.1029/2002JA009355